**DEVELOPMENT OF A FLAPPING WING DESIGN INCORPORATING
SHAPE MEMORY ALLOY ACTUATION**

THESIS

Jeffery A. Barrett, Lieutenant Commander, USN

AFIT/GAE/ENY/10-M02

**DEPARTMENT OF THE AIR FORCE
AIR UNIVERSITY**

AIR FORCE INSTITUTE OF TECHNOLOGY

Wright-Patterson Air Force Base, Ohio

AFIT/GAE/ENY/10-M02

**DEVELOPMENT OF A FLAPPING WING DESIGN INCORPORATING
SHAPE MEMORY ALLOY ACTUATION**

THESIS

Presented to the Faculty

Department of Aeronautics and Astronautics

Graduate School of Engineering and Management

Air Force Institute of Technology

Air University

Air Education and Training Command

In Partial Fulfillment of the Requirements for the

Degree of Master of Science in Aeronautical Engineering

Jeffery A. Barrett, BS

Lieutenant Commander, USN

March 2010

AFIT/GAE/ENY/10-M02

**DEVELOPMENT OF A FLAPPING WING DESIGN INCORPORATING
SHAPE MEMORY ALLOY ACTUATION**

Jeffery A. Barrett, BS

Lieutenant Commander, USN

Approved:

_____/signed/_____   _____
Black, Jonathan T., Civ AFIT/ENY (Chairman)   Date

_____/signed/_____   _____
Reeder, Mark F., Civ AFIT/ENY (Member)   Date

_____/signed/_____   _____
Cobb, Richard G., Civ AFIT/ENY (Member)   Date

AFIT/GAE/ENY/10-M02

Abstract

This research sought to validate a proof of concept regarding shape memory alloy actuation of a flapping-wing blimp. Specimen wires were subjected to cyclic voltage at increasing frequencies to quantify expected strains. A laser vibrometer captured 2048 sample velocities during single contraction and elongation cycles, and the resulting samples were used to calculate displacements. Displacements were determined ten times for each specimen and frequency to compute averages. Subsequently, a circumventing frame was designed to encase a blimp envelope and provide support for a flapping motion actuation system. Contraction of shape memory wire translated force to the flapping mechanism via bellcranks, pushrods, and clevises, while bias springs promoted elongation of the wire during power-off phases.   Performance characteristics of the flapping system, augmented with each specimen wire individually, were determined during bench-top testing.

A modified frame design was constructed when it was determined that the weight of the prototype exceeded the buoyant force of the blimp envelope. The modified frame was later fitted to a larger blimp envelope, because it too exceeded the weight restriction of the original envelope.   Subsequently, a circuit was constructed to cycle voltage at 0.2 hertz as applied to the actuating specimen wires, and performance of the system observed with the incorporation of each specimen. The modified prototype showed optimum performance of 25 to 35 degrees wing deflection while incorporating a 0.005 inch diameter shape memory wire.

Acknowledgments

Table of Contents

List of Figures

List of Tables

DEVELOPMENT OF A FLAPPING WING DESIGN INCORPORATING SHAPE MEMORY ALLOY ACTUATION

I. Introduction

Motivation

During the twentieth century, mankind's endeavors within the domain of flight achieved an unprecedented rate of technological advancement paralleling that of the industrial revolution. Inaugurated at Kitty Hawk, the age of flight subsequently witnessed the advent of jet propulsion, development of stealth, and the mastery of extraplanetary travel. While these historic advancements encapsulate the achievements of manned flight, the past two decades testify to the aspired augmentation of unmanned systems within the flight domain. With the continued proliferation of unmanned systems such as the MQ-1 Predator, battlefield commanders are dispensed the beneficial mitigation of casualty risk associated with piloted systems. The unmanned system provides a relatively expendable platform to infiltrate areas of robust and pernicious defense and is increasingly viewed as the core architecture of future combat. A crucial functional component of this architecture is reconnaissance. While larger scale unmanned aerial vehicles like the Predator function well within the broad range sectors defining conventional combat, their size, maneuverability, and speed preclude tasking within the confines of urban warfare. In response to the expanding influence of urban warfare, micro air vehicles will provide the predominate means to the reconnaissance mission.

Research Focus

The project chronicled in this thesis sought to qualitatively asses a micro air vehicle proof-of-concept incorporating an unconventional method of flapping wing actuation. Flapping motion has historically presented an arduous challenge to the micro air vehicle community. Actuator complexity, low Reynolds number aerodynamics, volume constraint, stability, control, and component miniaturization are just a sampling of the factors governing the viability of such a system. While each factor alone can critically undermine functionality and performance, the purpose of this conducted research was not the optimization of each. Research was focused on the feasibility of smart memory alloy actuation with regard to flapping motion. While weight reduction was a predominate motivation for the smart memory alloy actuation method, optimizing the weight characteristics of other components was accomplished superficially. The research and methods required to tactically optimize the weight characteristics of such components as power supply and circuitry were well beyond the scope of this project, as was the optimization of wing aerodynamics. The project was an exposé on decreasing the complexity of a flapping wing actuation system, reducing the weight allocation of such mechanism, validating a proof-of-concept, and providing shape memory alloy kinematic data that could be used to optimize future designs.

Document Organization

The succeeding sections of this document are delineated as follows: Literary Review, Methodology, Analysis and Results, Conclusions and Recommendations, and

Appendix. The Literary Review is subdivided into sections that substantiate the selection of a flapping wing design, characterize the influence of weight, describe the detriments of common drive mechanisms, justify the shape memory alloy approach, illustrate the shape memory effect, and validate a blimp platform. The Methodology section describes the manner in which functional kinematics of Nitinol were determined, the design and fabrication methods associated with the prototype system, and how the prototype response was tested. Analysis and results include the behavioral characteristics of shape memory alloy specimens, the observed response of the prototype to specific specimens, and resulting system refinement. The Conclusions and Recommendations section presents synoptic precepts associated with shape memory alloy actuation, as well as recommendations for future research. Finally, the Appendix includes the Matlab codes employed in the specimen wire stroke analysis as well as displacement results for each specimen.

II. Literature Review

Flapping Wing Attestation

For ages, man has looked to the sky and paid contemplative curiosity to the many creatures actively defying the law of gravity. This inquisitive fascination has been manifest from the legend of Icarus within Greek mythology to the avant-garde research and development of today. While early flight attempts are often viewed as an amalgamation of unorthodox and recurrently-failed experimentation, the preponderance of mechanisms today have solidified into two viably tested approaches: fixed and rotary wing designs. These designs offer practical, dependable, and certain solutions with regard to a macro-scale flying system. The scale of this type system is dictated by the lower bound size requirements imposed by the need to carry passengers, weapon systems, or large payloads, and thus the employment of these macro-scale flying systems generally necessitates designs driven by a balance of speed, range, as well as volumetric and load carrying capacity (Kroo and Kunz, 2001: 504). However, the realm of flight has recently witnessed a vectored interest toward that of the low cost, micro-scale, unmanned flying system capable of sensor deployment (Mueller and DeLaurier, 2001: 2).

While fixed and rotary-wing designs suffice for implementation within macro-scale flight systems, the functional propositions of micro-scale flight systems are often at odds with inherent characteristics of these designs. Robert C. Michelson contends that vehicles tasked with reconnaissance and surveillance missions must adapt to the now prominent arena of urban warfare. His premise is that current fixed-wing Unmanned

4

Aerial Vehicles (UAV's) are not adept within this setting due to their dependence on either large wings or relatively high speed required to sustain flight. He concludes that a functional design must be capable of slow flight and maneuverability within constricted areas in order to "…stop, look into windows, or even land in tight spaces to place sensors" (Michelson, R. C., 1999:5). Additionally, aerodynamic studies of biological flyers have led to the observation that smaller aspect ratio wings generally correlate to greater maneuverability and agility (Shyy and others, 2008: 19). Thus, the functional ability to maneuver and operate within confined spaces requires relatively small wings with significantly smaller aspect ratios (Torres and Mueller, 2001: 116), as well as reduced airspeeds that are typically not conducive to fixed wing flight. Subsequently, Michelson turns his examination to the prospect of rotary versus flapping-wing design. His first argument asserts that a flapping wing has a greater endowment to recover potential energy by configuring to a "nonflapping glide" than does a rotary wing in autorotation (Michelson, R. C., 1999: 7). This endowment affords the flapping wing a nominal facet of endurance and energy conservation. Second, he maintains that the rate of control inputs for a flapping wing is reduced in comparison to that of a rotary wing (Michelson, R. C., 1999: 7). Consequentially, stability and control components can be simplified and tapered in terms of size and weight. Michelson also cites the beneficial acoustic stealth properties of the flapping wing over the rotary design. He contends that as the size of a rotary design vehicle is reduced, the efficiency of the rotor is diminished. This necessitates a higher angular velocity of the blades, thus increasing the acoustic signature in both frequency and energy (Michelson, R. C., 1999: 7). While it has been

shown that the upper and lower bound wing-beat frequencies of a flapping design vary

inversely with mass (Shyy and others, 2008: 20), and thus smaller size requires a higher

flapping frequency, Michelson poses the following counter:

> …the energy will be expended over a wider acoustic bandwidth, but unlike
> the rotorcraft, it will be nonuniformly distributed in the horizontal plane.
> The net result is that a flapping wing approach will be less noticeable than
> a rotary wing approach because the sound spectrum produced will
> approximate wide band white noise rather than a discrete tone (Michelson,
> R. C., 1999: 7).

Many researchers echo Michelson's attestation to the ascendency of flapping-wing

designs over fixed and rotary-wing designs within the domain of micro-scale systems.

The benefits of the flapping-wing approach is perhaps best abridged by Othon Rediniotis

and Dimitris Lagoudas in the statement "A significant advantage of flapping wing

propulsion is that lift can be generated with little or no forward velocity and with small

wing size" (Rediniotis and Lagoudas, 2001: 484). The previous arguments present a

sound deduction that a functional micro-scale design should incorporate a flapping-wing

mechanism; however, the development of such a propulsive device continues to present

conventional impediments commonplace within the micro-scale domain. Two most

notable and ubiquitous of these challenges are the attenuation of weight and complexity

of design.

Weight Factor

The most pronounced hurdle to miniaturization of a flapping-wing flyer involves weight curtailment of components and the system as a whole. Michelson upholds weight reduction as "the most critical factor in creating a successful MicroFlyer," (Michelson, R. C., 1999: 8). In fact, a system's comprised weight is shown to have dramatic influence over power requirements. Akira Azuma quantified this influence in his derivation of the equation for specific power (necessary power to weight ratio) required in horizontal flight of a flapping system (Azuma, A., 2006: 137):

$$\frac{P_n}{W} = \frac{P_o}{W} + \left(\frac{C_{D_o}^{\ 2}}{\pi\,AR} + C_{D_o}\right)\frac{\rho/2}{W/S}U^3 + \frac{1}{\pi\,AR}\left(1 + \frac{2C_{D_o}}{\pi\,AR}\right)\frac{W/S}{\rho/2}\frac{1}{U} + \frac{1}{(\pi\,AR)^3}\frac{(W/S)^3}{(\rho/2)^3}\frac{1}{U^5} \qquad (1)$$

where

P_n = Necessary Power for horizontal flight

W = Weight

P_0 = Power required to overcome profile drag of wings

C_{D_0} = Parasite Drag Coefficient

AR = Aspect Ratio

ρ = Fluid Density

S = Planform Area

U = Flight Speed

Solving for necessary power, and simplifying:

$$P_n = P_o + \frac{C_{D_o}{}^2 \rho S U^3}{2\pi\, AR} + \frac{C_{D_o} \rho S U^3}{2} + \left[\frac{2}{\rho S U \pi\, AR} + \frac{4 C_{D_o}}{\rho S U (\pi\, AR)^2}\right] W^2 + \left[\frac{8}{(\rho S \pi\, AR)^3 U^5}\right] W^4 \quad (2)$$

The necessary power, therefore, is comprised of two terms that are proportionally dependent on the second and fourth powers of weight. Given a system held constant in terms of size and aerodynamic parameters, it is evident that a reduction in weight affords a decrease in necessary power required for horizontal flight. This decrease translates to greater endurance given a defined energy source, or alternatively it allows for smaller energy capacity of a source given a defined endurance requirement.

Another germane repercussion of a flyer's weight involves the relation between wing loading and weight. Based on the variation of both wing area and weight with respect to characteristic length, a formulation regarding the interrelation between wing loading and weight can be derived as follows (Shyy and others, 2008: 16):

$$S \sim l^2$$

$$W \sim l^3$$

$$\frac{W}{S} \sim \frac{l^3}{l^2} = l$$

$$\frac{W}{S} \sim W^{1/3} \quad\quad\quad (3)$$

This one-third power dependence is universally characteristic of both man-made and natural flyers (Ho and others, 2003: 640). This dependence results in an interpolated line with slope of 0.33 when plotting the wing loading of various flyers versus weight, shown in Figure 1.
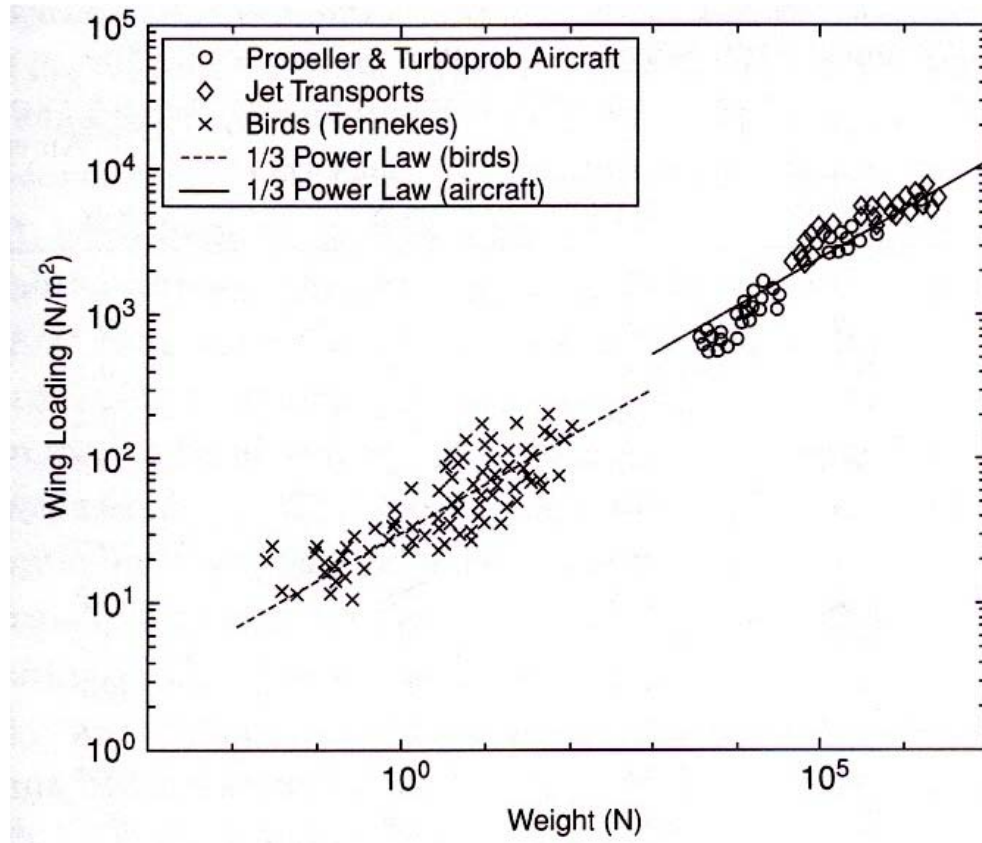
Figure 1. Wing Loading Versus Weight (Liu, T., 2006)

Based on this evidence, it has been concluded: "…there is a maximum weight that can be carried by a flyer of a certain size; or vice versa, a minimum size given a certain gross weight" (Ho and others, 2003: 640). Mueller and DeLaurier quantify the generally-applied fractional weight of micro air vehicle components to include a twenty-one percent weight allocation to airframe components, thirty percent to energy source components, twenty-one percent to payload components, seventeen percent to avionics components, and eleven percent to propulsive components (Mueller and DeLaurier, 2001: 4). In addition to the afforded benefits of weight reduction examined previously,

9

reducing the weight of one of these components grants an optional weight trade towards other components if the vehicle is designed under defined weight and size requirements.

Issue of Drive Mechanism

Flapping wing design necessitates lever-type translation of the wings. This action is generally devised by first-class or third-class levers in which the pivot point is between the input force and the wingtip, or the input force is between the pivot point and wingtip respectively. The points of contention regarding this action in flapping wing design are the complexity and weight of the actuating system. Numerous devices have been constructed in an attempt to engage the lever-type translation. The preponderance of these devices model an electric motor that produces a rotational force translated into linearly reciprocating motion via crankshaft interaction. Figures 2 and 3 illustrate one device, called a four-bar mechanism, that incorporates this concept.
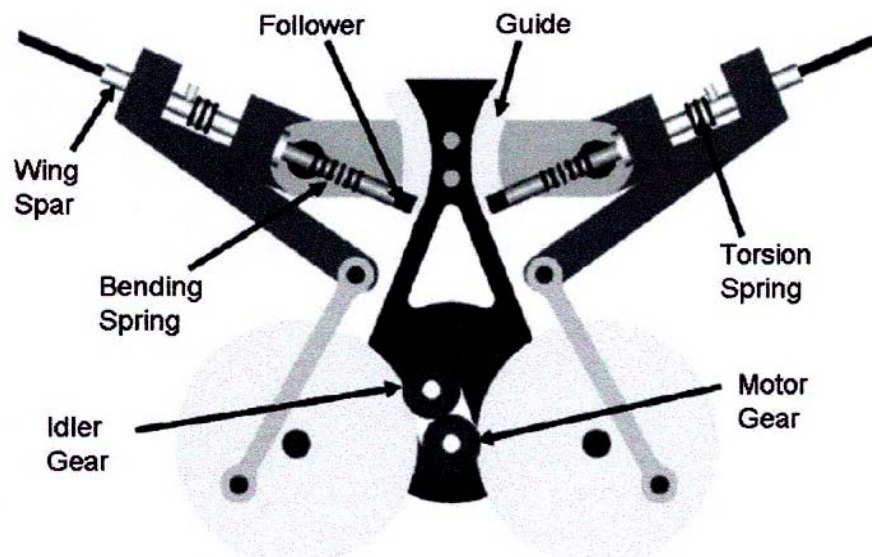
Figure 2. Four-Bar Mechanism (McIntosh et al, 2006: 147)

Figure 3. MHP III Incorporating Four-Bar Mechanism (McIntosh et al, 2006: 146)

The prototype depicted in Figure 3, dubbed MHP III, embodies the complexity associated

with translation of rotary motion to linearly reciprocating motion. Likewise, the MHP III

has a weight of 50 grams (McIntosh et al, 2006: 147). Considering the previously cited

fractional weight allowance of propulsive components as set forth by Mueller and

DeLaurier, the 50 gram weight of the MHP III would stipulate a 455 gram gross weight

for the entire micro-air vehicle and substantially eclipse the 100 gram vehicle weight

limit established by Spedding and Lissaman (Spedding and Lissaman, 1998: 458).

Moreover, constraining the system's gross weight to 100 grams would emphatically

abridge the weight allowances ascribed to airframe, energy source, payload, and avionics

components. An additional representation of the rotary driven method is illustrated in

Figure 4.
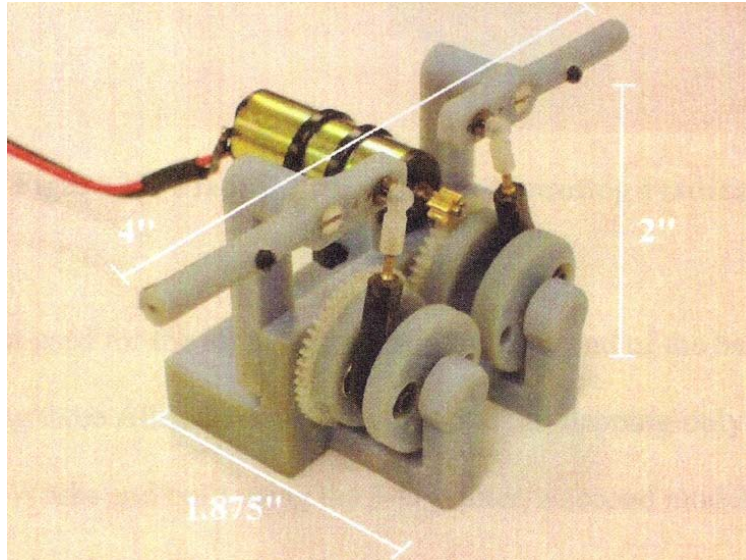
Figure 4. Svanberg Flappping Mechanism (Svanberg, C. E., 2008: 33)

While Svanberg's mechanism can be characterized as a bench-top design, the complexity of design persists. Additionally, the device weighs 44 grams, not inclusive of the 23 gram motor (Svanberg, C.E., 2008: 33). As a final exposé regarding the symptomatically adverse weight characteristics of the rotary driven approach, Jadhav's mechanism depicted in Figure 5 exhibits a combined weight of 45 grams for the flywheel, crankshaft, and connecting pins alone, while the required driving motor measures 128 grams (Jadhav, G., 2007: 33).
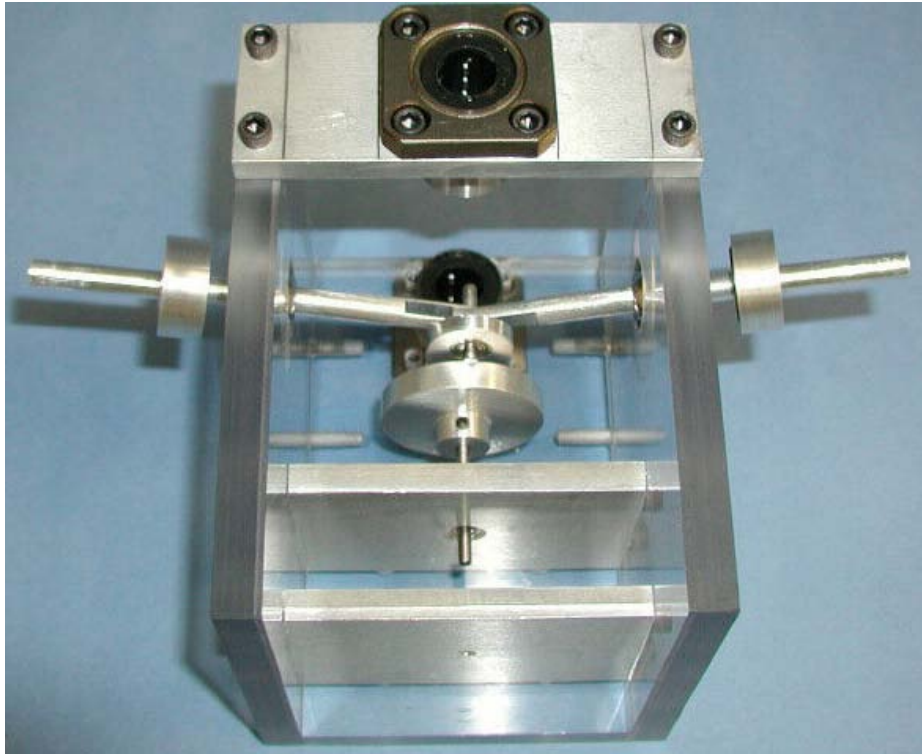
Figure 5. Jadhav Flapping Mechanism (Jadhav, G., 2007: 28).

Mechanisms that adopt the rotary driven actuation trait subsume innate complexity, consume valuable space, and retain pernicious weight fractions within the limited volumetric constraints of a micro-scaled flyer. Considering the detrimental consumption of volume and weight allowances, these actuating systems concede sparse sanctions for payload and control systems (Rediniotis and Lagoudas, 2001: 484). Conclusively, a functionally-viable micro-scale flapping vehicle necessitates a simplistic and light weight propulsive mechanism.

Shape Memory Alloy Approach

As the scale of a flying system is diminished, it becomes necessary to devise propulsive components of smaller size and weight while retaining favorable force outputs. One solution common to micro-actuators has been the supplanting of conventional motors with piezoelectric actuators. While decreasing the encompassing size and weight of the actuating system, the associated deficiencies of this approach include limited strain generation and the requirement of high driving voltage (Lan and others, 2009: 258). However, recent advances in the material sciences have demonstrated promising potential utilizations within the domain of micro-systems; foremost among these advances is the field of Shape Memory Alloys. Shape memory alloys are those that exhibit the Shape Memory Effect. Comparing against motor-based actuation systems, smart memory alloys offer simplicity, compactness, and higher energy densities (Seow and others, 2008). With regard to piezoelectric actuators, shape memory alloys are capable of larger strain displacements as well as larger forces (Song and others, 2003: 224). In fact, Kohl contends:

> Among the presently known actuation principles, the shape memory effect shows the highest energy densities, which are on the order of 10 J/cm^3 for NiTi alloys. For this reason, the shape memory effect appears particularly interesting for applications where, despite small dimensions, large forces and displacements are required (Kohl, M., 2004: 3).

Because of the large force generation resulting from minimal energy input, shape memory alloys have recently become the focused actuation technique within the domain

14

of micro design (Ohkata and Suzuki, 1998: 264). Comprehensively, the shape memory

effect can be described as the proclivity of a deformed specimen to recover an initial,

unstrained shape when triggered thermally or mechanically (Kohl, 2004: 25), and the

means of this shape retention is best understood from an atomic view.

Shape Memory Effect

Many alloys exhibit the Shape Memory Effect with an associated superlattice

structure. The compositional array of shape memory alloys are cardinally classified as

face-centered cubic or body-centered cubic in consonance with the sublattice structure of

their parent (austenite) phase (Miyazaki, 1996: 72). While the austenite sublattice unit

cell of a few shape memory alloys exhibit fourteen lattice points arranged about the

surface and points of a cube (face-centered cubic), Miyazaki stipulates that face-centered

cubic orientation is a rarefied construction applicable to the ferrous alloys (Miyazaki,

1996: 72-73).   The preponderance of shape memory alloys are categorized as β-phase

alloys in which the unit cells demonstrate body-centered cubic (BCC) structure

characterized by nine lattice points. Eight of these lattice points manufacture an

archetypal cubic structure while the ninth is centrally imbedded. β-phase alloys are

further segmented based upon element ratio within the superlattice structure: β2-phase

denoting an approximate 50:50 elemental composition ratio and β1-phase marking a ratio

of 75:25 (Miyazaki, 1996: 73). Figure 6 depicts four adjacent unit cells of β2-phase

nickel-titanium (NiTi) shape memory alloy in the austenitic state.
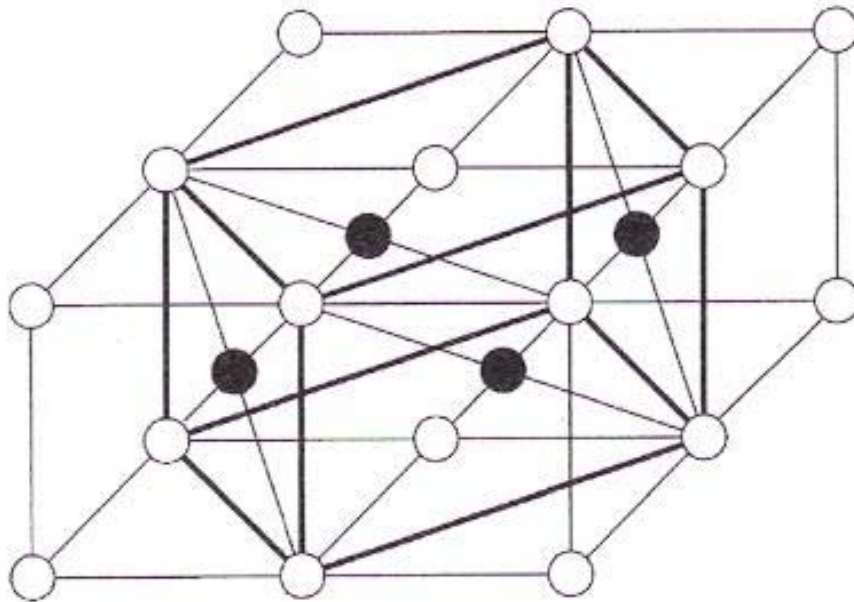
Figure 6: Four Unit Cell NiTi (Kohl, 2004: 30)

Cooling an austenitic phase specimen below a defined transformation temperature allows a martensitic transformation to begin. Conversely, heating a martensitic phase specimen above a defined temperature elicits a phase transformation to austenite. Under martensitic transformation, a stressed lattice structure deforms in a shear fashion attributed to concerted lattice point movements resulting in strain (Shimizu and Tadaki, 1987: 1). Kohl quantifies the lattice point displacements of NiTi in Table 1 below as they physically correlate to Figure 7.

Table 1: NiTi Lattice Parameters (Kohl, 2004: 30)

Lattice parameter	Martensite	Austenite
a	0.2898 nm	0.3015 nm
b	0.4108 nm	0.4263 nm
c	0.4646 nm	0.4263 nm
α	90°	90°
β	97.78 °	90°
γ	90°	90°
V	54.79×10^{-3} nm^3	54.78×10^{-3} nm^3
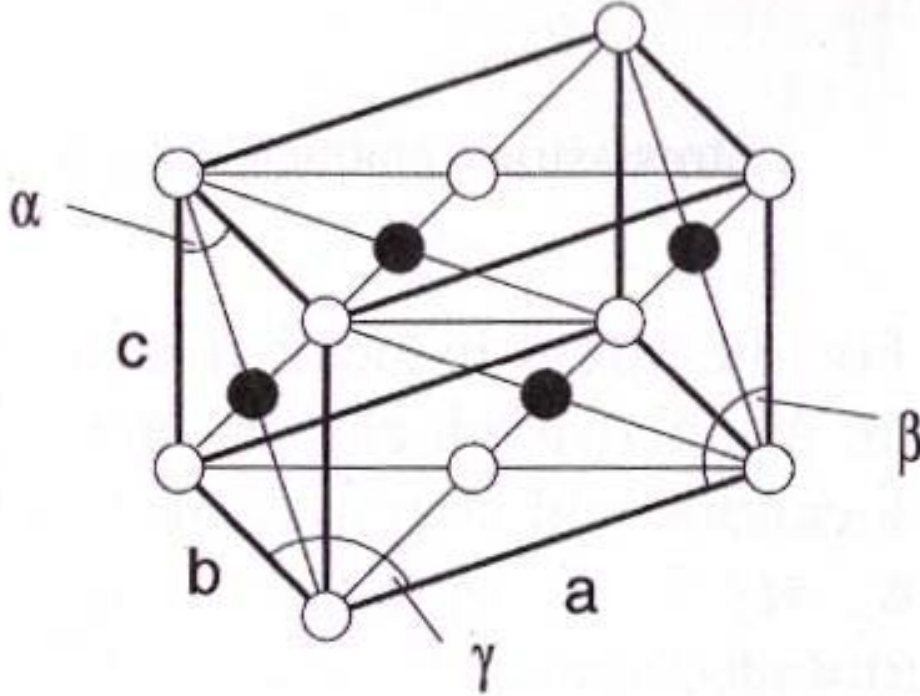
Figure 7: NiTi Lattice Parameter Assignments (Kohl, 2004: 30)

While experimentally determined martensitic lattice parameters of NiTi vary, distance parameters only show a variance on the scale of thousandths of an angstrom.

Additionally, variance among experimentally-determined angular parameters is observed only within the valuation of the β parameter and is on the scale of a single degree (Shimizu and Tadaki, 1987: 63).

Cooling an austenitic phase specimen below a defined transformation temperature allows the martensitic transformation to begin. Conversely, heating a martensitic phase specimen above a defined temperature elicits a phase transformation to austenite. Neither transformation process is instantaneous, but rather, occurs fractionally within the specimen over a transitory temperature range. As a martensitic phase specimen is heated, the fractional constitution transformed to the austenite state increases from zero to one over a defined temperature range (Birman, V., 1997: 629). This transformation initiates at the austenite start temperature (A_s) and culminates when the elevated austenite finish temperature (A_f) has been realized (Birman, V., 1997: 629). An analogous process transpires within the transformation from austenite to martensite. In this case, a fully austenitic phase specimen undergoes a fractional transition to the uniform martensite state, initiated in conjunction with the martensite start temperature (M_s) and effectuated at the lower martensite finish temperature (M_f) (Birman, V., 1997: 630). Figure 8 outlines the transitional stages as martensitic fraction of the specimen versus temperature.
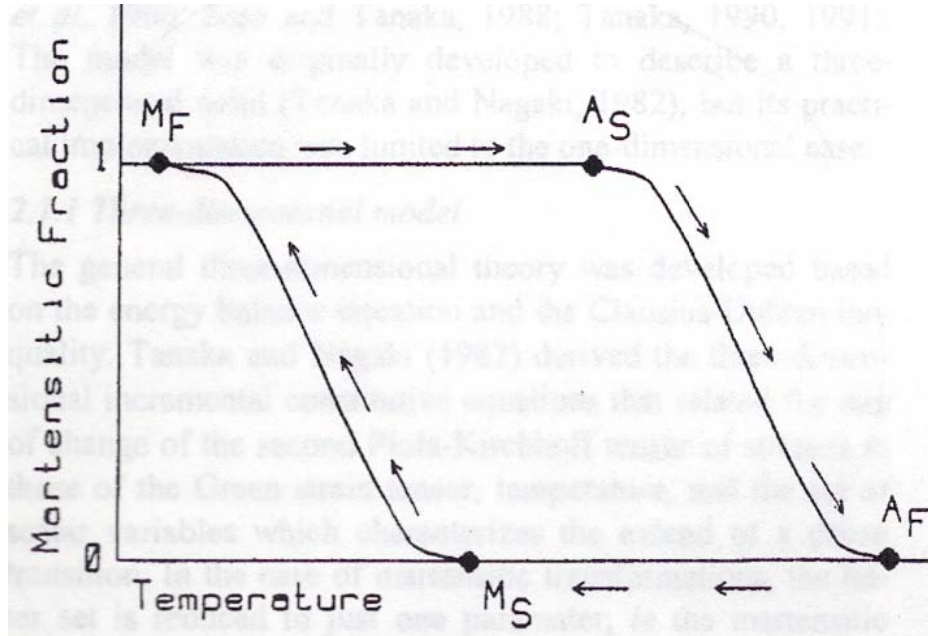
Figure 8. Martensitic Fractional Variation (Birman, V., 1997: 630)

While temperature transition induces phase transformation, the process does not

singularly effect deformation. To generate advantageous strain, a load application is

required. Comparing the yield limit of a martensitic phase specimen to that of an

austenitic phase specimen, Birman chronicles the former to be much lower than the latter.

Thus as a loaded specimen is cooled to martensite, a relatively large plastic deformation

is realized (Birman, V., 1997: 629). Analysis by Honma demonstrates a linear

correlation between the yield stress and specimen temperature of several β2-phase NiTi

alloys as represented in Figure 9.
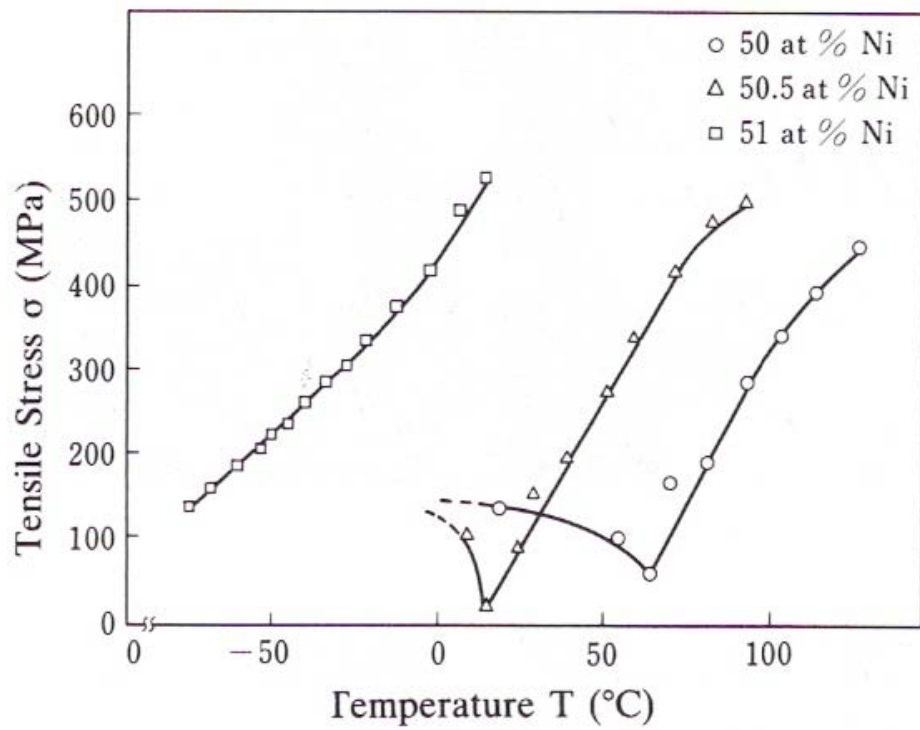
Figure 9. NiTi Yield Stress Versus Temperature (Honma, T., 1987: 79)

Given the linear correspondence, it can be surmised that yield stress varies in proportion

to the martensitic fraction of the specimen. Many sources ostensibly reach the same

corollary, and revise the cycle of Figure 8 as a presentation of specimen length versus

temperature (Seow and Liu, 2008:2; Song and others, 2003:225).
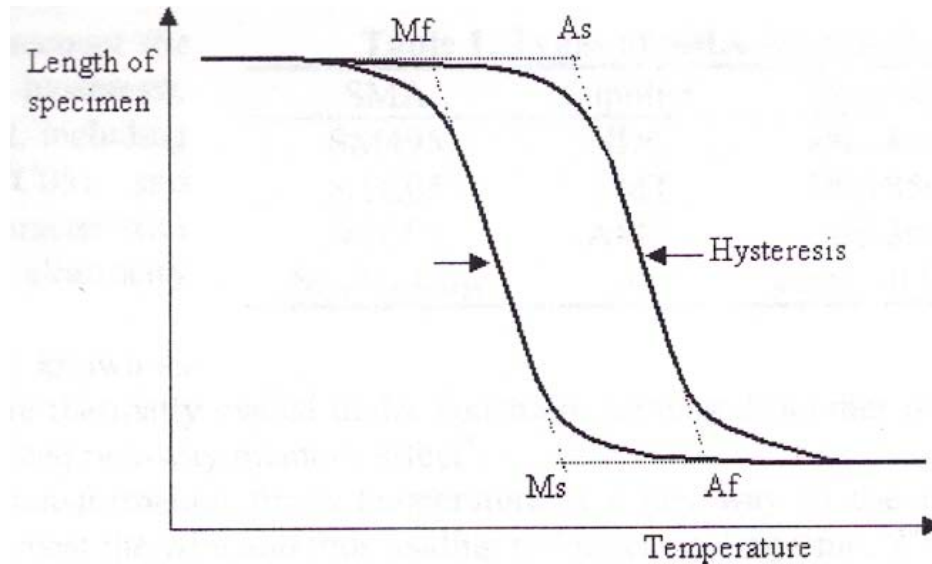
Figure 10. Wire Length Versus Temperature (Seow and Liu, 2008:2)

The primary limitation of shape memory alloy implementation is the rate at which the alloy cools after thermal excitation has been removed. Once a strained specimen has traversed to an unstrained state via thermal addition and the source of thermal addition has subsequently been removed, it becomes necessary to discharge the latent heat from the alloy in order to achieve the strained condition once more. Conventional SMA actuator designs rely on convection to dissipate this heat from the alloy, thus enabling strain once again in the specimen via a bias force. It becomes axiomatic that cyclic actuation rates form a direct dependence on the rate at which the alloy cools. While cooling rates and thermodynamic inefficiencies tend to effectuate marked liabilities to macro-scale SMA actuators, Kohl concludes that the detriment imposed by these factors becomes much less pronounced as the scale of the actuator is decreased (Kohl, 2004: 3). The less pronounced effects of cooling rate and thermodynamic inefficiency within a

21

micro-scale SMA actuator can be credited to the larger surface-to-weight ratio which
facilitates convection (Ohkata and Suzuki, 1998: 264).

Blimp Platform

Given the advantages of flapping wing design, as well as the simplicity and
weight reduction afforded by shape memory actuation, it is surmised that together they
provide a pragmatic means of micro air vehicle propulsion. This project sought to
incorporate both shape memory alloy actuation and flapping design within the confines of
a blimp platform. Advantages of the blimp platform include payload capacity, stability,
endurance, and decreased noise (Brandreth, 2000: 1884). Additionally, a blimp platform
decreases the required flapping frequency for flight. The buoyancy of the blimp provides
the lift. Because flapping motion is required only to propel the device, the flapping
frequency will be less than required to also produce lift. A novel concept of a flapping
blimp is the Festo Air_Ray, depicted in Figure 11.

Figure 11. Festo Air_Ray (Festo AG & Company)

The Festo Air_Ray utilizes a servo drive unit to actuate the flapping motion, spans 4.2 meters, and has a mass of 1.6 kilograms (Festo AG & Company). While the Festo Air_Ray integrates flapping wing propulsion with a blimp platform, it does not employ shape memory actuation. The project chronicled herein seeks to validate a proof of concept with regard to the coupling of shape memory actuation to a flapping blimp. Because the actuation mechanism is novel and innovative, a blimp platform was chosen as an intermediate step to test the design and provide lift. Future optimization of the design potentially lends itself to the achievement of pure flapping flight. While functionally similar to other blimp designs, the proof of concept uniquely incorporates shape memory actuation.

III. Methodology

Functional Kinematics of NiTi

The initial phase of the project was to determine the functional kinematics of Nitinol. The direction of this research aimed at quantifying the stroke length of selected diameter Nitinol wires as a function of cycling rate. Several Nitinol wires, trademarked as Flexinol[TM] and advertised as 50:50 Nickel-Titanium in composition, were purchased online from Dynalloy Incorporated. Ninety-degrees Celsius was the advertised transition temperature of the purchased specimens and their diameters included 0.0015, 0.002, 0.003, 0.004, 0.005, and 0.006 inches. Although Dynalloy Incorporated ostensibly advertises a distinct transition temperature, inspection of their technical data sheets revealed a martensite start temperature of 72 degrees Celsius, a martensite finish temperature of 62 degrees Celsius, an austenite start temperature of 88 degrees Celsius, and an austenite finish temperature of 98 degrees Celsius (Dynalloy Incorporated, http://www.dynalloy.com/pdfs/MWPBv4.00_FlexSpecs.pdf). Additional metrics are listed in Table 2 below. Note, the amperages associated with each wire represent an ideal constraint to avoid overheating and prevent permanent strain in the specimen.

Table 2. Flexinol Metrics (http://www.dynalloy.com/TechData.html)

Diameter Size (Inches)	Resistance (Ohms/Inch)	Maximum Pull Force (grams)	Approximate* Current at Room Temperature (mA)	Contraction* Time (seconds)	Off Time 70° C Wire** (seconds)	Off Time 90° C Wire** (seconds)
0.0010	45.0	7	20	1	0.10	0.06
0.0015	21.0	17	30	1	0.25	0.09
0.002	12.0	35	50	1	0.3	0.1
0.003	5.0	80	100	1	0.5	0.2
0.004	3.0	150	180	1	0.8	0.4
0.005	1.8	230	250	1	1.6	0.9
0.006	1.3	330	400	1	2.0	1.2
0.008	0.8	590	610	1	3.5	2.2
0.010	0.5	930	1000	1	5.5	3.5
0.012	0.33	1250	1750	1	8.0	6.0
0.015	0.2	2000	2750	1	13.0	10.0
0.020	0.16	3562	4000	1	17.0	14.0

A test specimen representing each wire diameter was prepared by cutting 100 millimeter long samples with wire-cutters. Terminal points were fabricated on the ends of each test specimen to provide an attachment point for bias loads as well as an attachment point to the test stand. These terminal points were fabricated from stainless-steel hypodermic tubing purchased from Small Parts Incorporated (http://www.smallparts.com/). Two separate dimensions were used, 26 gauge tubing with 0.018 inch outer diameter and 0.010 inner diameter as well as 22 gauge tubing with 0.028 inch diameter and 0.016 inch diameter. The 26 gauge tubing was used to fashion attachment points for the 0.0015, 0.002, and 0.003 inch diameter test specimens and the 22 gauge tubing was used to fashion attachment points for the 0.004, 0.005, and 0.006 inch diameter test specimens. The fabrication process involved cutting two sections, each measuring about 5 millimeters, of hypodermic tubing for each test specimen. For the test stand attachment

point, one section of tubing was simply crimped to the wire. Additionally for the bias

load attachment point, one section was crimped to the wire and the section subsequently

bent midpoint via needle-nose pliers to form a "V" shape. Figure 12 visually depicts the

completely fabricated test specimen of the 0.004 inch diameter wire.
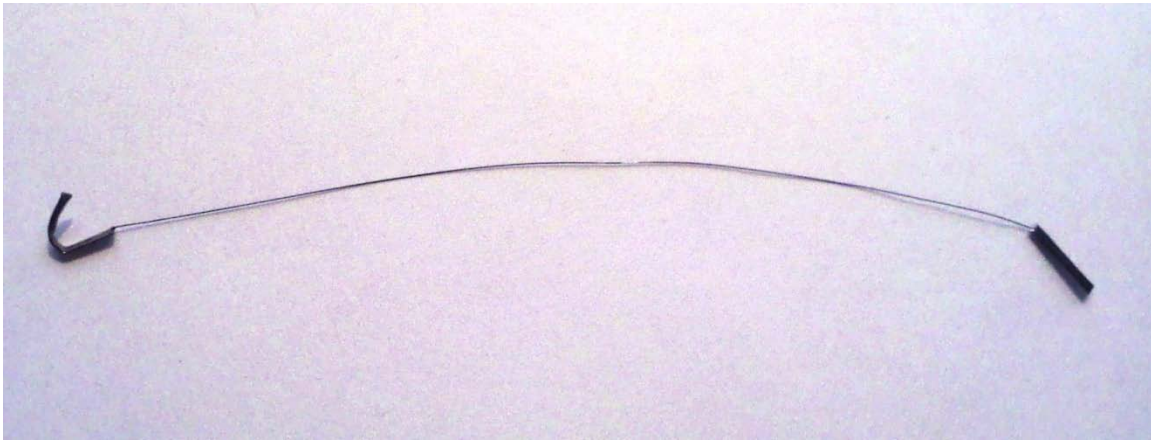
Figure 12. 0.004 Inch Diameter Wire Test Specimen

The test stand consisted of an elevated vise to which the attachment end of the test

specimen was clamped. The test specimen was hung vertically, and metric hanging

weights were fixed to the "V" shaped attachment end of each test specimen to provide

bias force. The selection of mass providing the bias force was governed in each case by

the maximum pull force denoted in Table 2, the increments of masses available, and the

need to minimize oscillation associated with multiple weights. Table 3 lists the selected

bias mass for each test specimen.

Table 3. Test Specimen Bias Mass

Wire Diameter (inches)	Bias Mass (grams)
0.006	300
0.005	200
0.004	150
0.003	75
0.002	20
0.0015	10

Electric current was the chosen method of actuation, and the resistance associated with each wire provided the process by which the austenite start and austenite finish temperatures were attained. Additionally, convection provided a simple and straightforward means to cooling the wire through the martensitic transformation. The voltage applied to each test specimen was calculated from the resistance data and ideal amperage data listed in Table 2. From Ohm's Law:

$$V = I*R \hspace{3cm} (4)$$

where V is the voltage measured in volts, I is the current measured in amperes, and R is the resistance measured in ohms. Table 4 depicts the variables and results of the ideal voltage calculation for each test specimen. Note, the length of the 100 millimeter test specimen was converted to inches to facilitate voltage calculation.

Table 4. Calculated Voltage Requirements

Diameter (in)	Ω/in	Length (in)	R (Ω)	I (amps)	V (volts)
0.006	1.3	3.937	5.1181	0.4	2.04
0.005	1.8	3.937	7.0866	0.25	1.77
0.004	3	3.937	11.811	0.18	2.12
0.003	5	3.937	19.685	0.1	1.96
0.002	12	3.937	47.244	0.05	2.36
0.0015	21	3.937	82.677	0.03	2.48

Power generation was provided by a Hewlett Packard 6236B Triple Output Power Supply and regulated by a Hewlett Packard 3312A Waveform Generator. A Tip31 transformer was necessary to interface the two components in order to increase the 20 milliamp output of the waveform generator to match that of the power supply. The configuration was designed and built by Air Force Institute of Technology lab technician Sean Miller, and viewed below in Figure 13. The power supply and regulation arrangement is depicted in Figure 14.
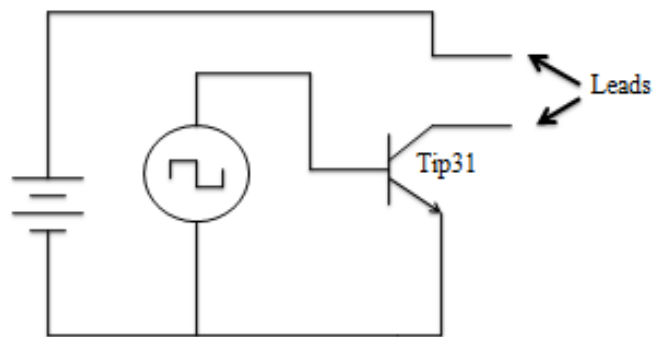
Figure 13. Power System Configuration
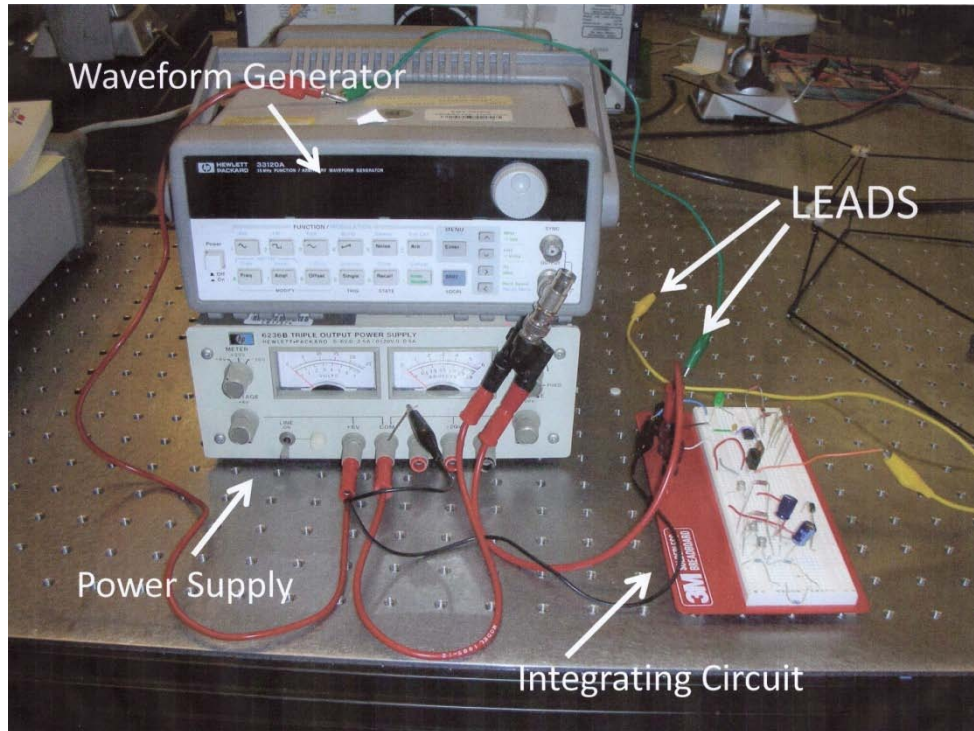
Figure 14. Power Arrangement

Testing of each specimen involved clamping one end to the vice, hanging the bias mass

to the "V" shaped termination point of the wire, fixing the power arrangement leads to

the termination points, and cycling the voltage to produce repeated contractions and

elongations of the wire. Determination of stroke length by visual means was deemed

subjective, sanctioning relatively large discrepancies between actual and observed

distances considering the scale of travel. Utilization of a laser vibrometer provided

salient objectivity to the measuring process. The laser from the vibrometer sensor head

was directed at a mirror. The incident reflection of the laser from the mirror was aimed at

the bottom of the bias mass hanging from the test specimen. Reflective tape was affixed

to the underside of the bias mass to provide adequate signal return. Figure 15 depicts the

set up excluding lead attachments from the power arrangement to the terminal points.
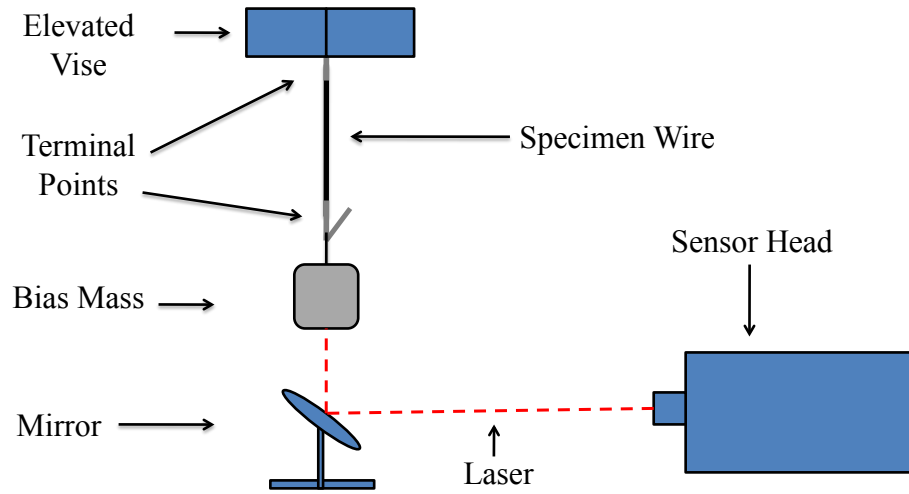
Figure 15. Testing Arrangement

The vibrometer system consisted of a Polytec OFV-505 Sensor Head and a Polytec

OFV-5000 Vibrometer Controller pictured in Figures 16 and 17 respectively.

Figure 16. Vibrometer Sensor Head

Figure 17. Vibrometer Controller

The vibrometer controller provided velocity output at a range setting of 10 mm/s/V and maximum frequency setting of 250 kHz. Tracking, low-pass, and high-pass filters were selected off. The software used to capture the resulting data was SignalCalc 620 Dynamic Signal Analyzer distributed by Data Physics Corporation.

Once the set-up was complete, the leads from the power arrangement were fixed to the attachment ends of the test specimen. Amplitude setting of the waveform generator was 2.5 volts peak to peak (VPP), and Offset was fixed at 1.25 VPP. The waveform was set as a 50% duty cycle square-wave, and the initial frequency setting was 0.1 Hz. Once the power supply was turned on, a multimeter was used to determine the voltage across the terminal points of the test specimen. The voltage output of the power supply was then adjusted until the voltage across the terminal points equaled the test specimen's calculated voltage requirement listed in Table 4.

Within the SignalCalc 620 software, "Transfer Function" was selected as the test type, and time domain settings were utilized. Block size was set at 2048 to give the

equivalent number of samples over the time range. From the "signal map" field, X2 was

selected as a Matlab file to be exported. Figure 18 is a screenshot of the software.
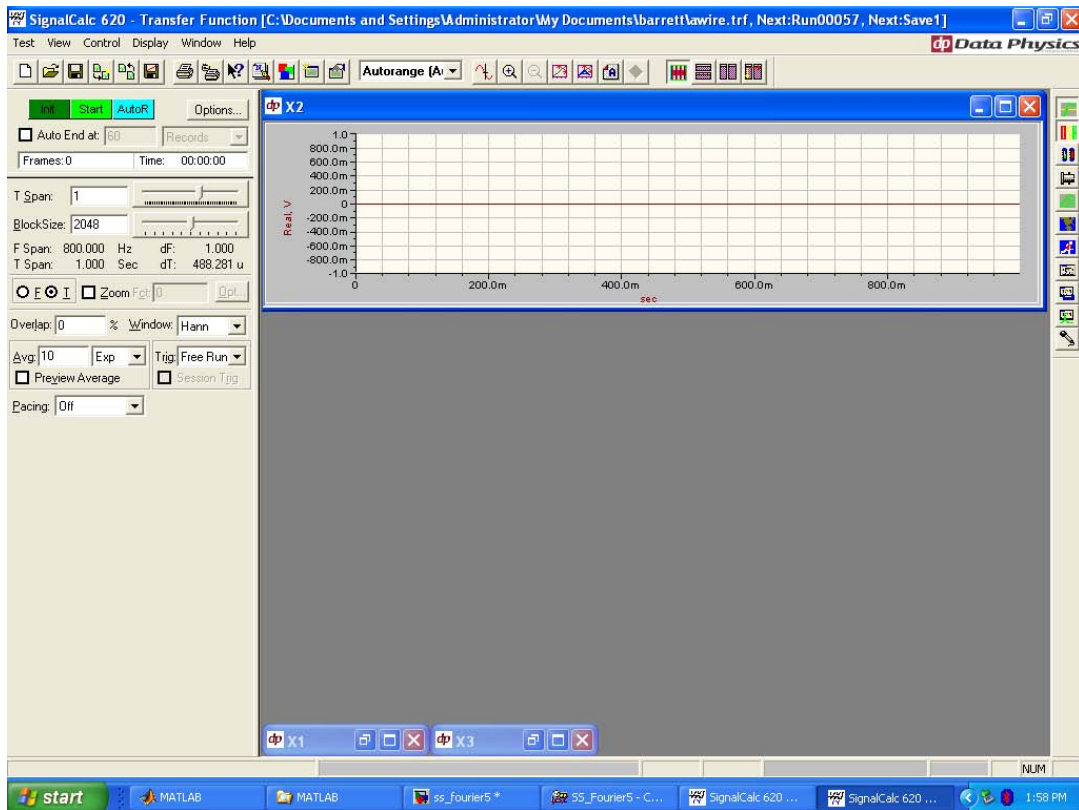
Figure 18. SignalCalc 620 Representative Screen

Time span was set to capture one cycle of test specimen movement through the

contraction and elongation stages associated with the austenitic and martinsitic

transformations. As the wire contracted and elongated, the SignalCalc 620 software

would capture 2048 velocity samples over the selected time interval. The software only

allowed the selection of predefined time intervals, and the selected value was chosen to

correspond with the period of motion as precisely as possible.

After software settings were accomplished, the data collection process began and was repeated for each test specimen. This process involved taking velocity samples over a range of a single cycle beginning with a frequency of 0.1 Hz as set by the waveform generator. Samples were taken at increasing 0.1 Hz steps until the test specimen produced little to no movement, and for each frequency setting, ten samples were taken to later determine an average displacement. Once data collection was complete, the data were exported as Matlab M-files, and the M-files were processed by the generated Matlab code included in Appendix A. Output of the Matlab code provided a plot of velocity versus time, displacement versus time, and stroke length as determined from peak-to-peak displacement. The ten peak-to-peak displacements associated with each frequency were averaged, and the average values were plotted versus frequency for each test specimen. Figure 19 depicts an example velocity versus time plot for the 0.003 inch diameter test specimen at 0.2 Hz, and Figure 20 depicts the displacement versus time plot. Note, positive velocities correspond to elongation associated with martensitic transformation of the test specimen, and negative velocities correspond to contraction of the test specimen associated with austenitic transformation.
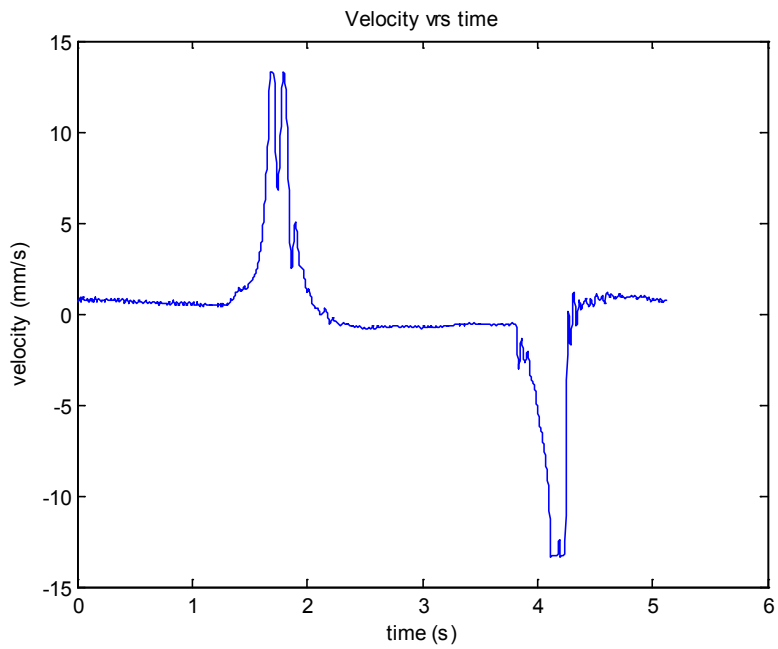
Figure 19. Matlab Plot of Velocity Versus Time
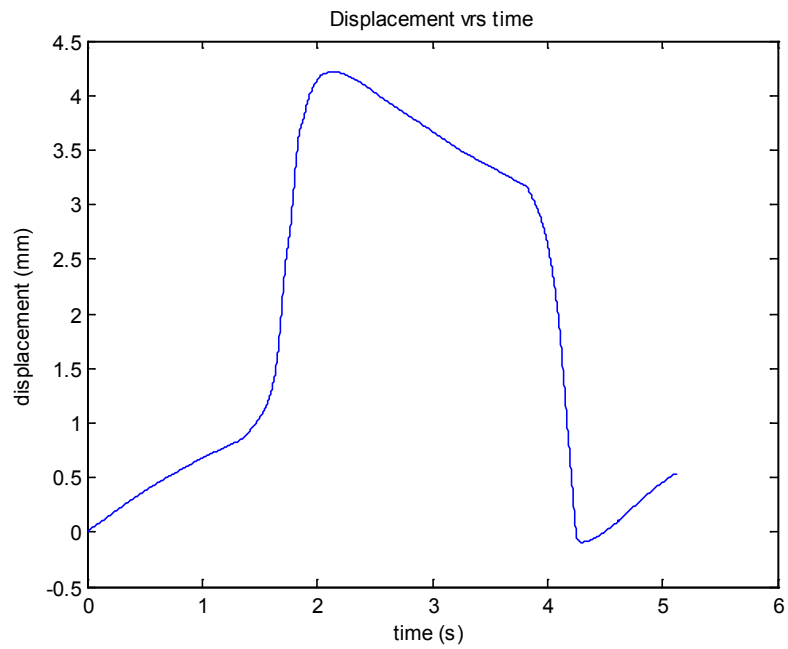
Figure 20. Matlab Plot of Displacement Versus Time

34

Results of the wire testing phase provide data upon which selection of wire diameter can be optimally determined given frequency specifications of flapping motion. Additionally, the test specimens were 100 millimeters long and subjected to ideal voltage. Therefore, the average displacement for a given frequency is equal to the percent strain expected in specimens of differing lengths when subjected to an ideal voltage. The ideal voltage of longer and shorter specimens can be calculated by multiplying the resistance per inch given in Table 2 by the specimen length, the product of which is multiplied by the amperage also listed in Table 2.

Prototype Frame and Actuator Construction

The decision to implement a shape memory alloy action system within the confines of a blimp-type micro air vehicle inaugurated a multifaceted challenge. Taking into account such factors as weight, number of components, strength, and performance, the project began to manifest itself as an enterprising trade study. The design not only had specific weight constraints as governed by the buoyant force of the blimp envelope, but also required structural rigidity that could antagonistically compete with weight requirements. Increasing the number of components required in the actuation system would also precipitate an accession of gross weight. Performance optimization, as governed by Nitinol wire diameter, presented a conflicting relationship between flapping frequency and magnitude of wing translation. Additionally, each wire necessitated unique power requirements that portended variations in power components.

The design process evolved around a silver metalized nylon blimp envelope distributed by Plantraco Microflight and available at the website: http://www.microflight.com/Online-Catalog/R-C-Toys/Balloon-24-for-MicroBlimp. The envelope, depicted in Figure 21, is a replacement for the distributer's advertised "MicroBlimp" depicted in Figure 22, which is a remotely controlled system that incorporates twin rotors for propulsion, and has a 24 inch envelope with an inflated diameter of about 18 inches. A previously purchased "MicroBlimp" was disassembled, and the component weights included 7.36 grams for the circuitry, motors, and propellers, 2.67 grams for the plastic gondola, 3.2 grams for the 3.7 Volt Lithium polymer battery, and 5 grams of ballast in the form of washers.

Figure 21. Blimp Envelope

Figure 22. MicroBlimp (http://www.microflight.com/Online-Catalog/R-C-

Toys/MicroBlimp-RTF-Set)

A paramount hurdle of the design process was how to physically integrate a

flapping mechanism to the blimp envelope. Initial design concepts supposed that the

components be adhesively fixed to the envelope itself as represented in Figure 23. The

design would require four hinge points physically attached to the envelope via epoxy and

the envelope itself would be the frame of the design. While this approach appeared

superficially feasible, further inspection revealed that the non-rigid blimp envelope

provided little supportive strength and would deform during actuation, impeding the

flapping motion.
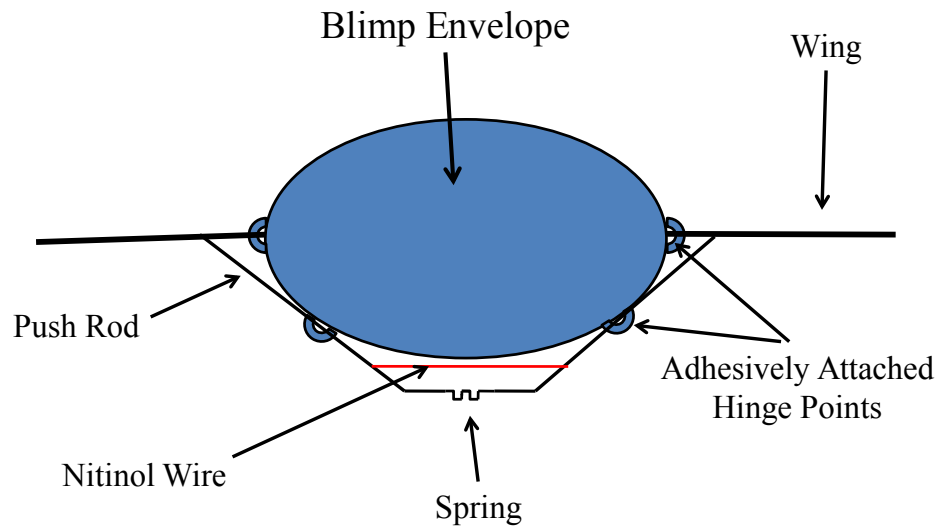
Figure 23. Initial Concept

Acknowledging the need for supportive rigidity, the adjudicated resolution was to encase the blimp envelope within a structural frame and mount the actuation system to the frame. While balsa wood could provide a stronger framework than the envelope, a balsa compositional frame was deemed too brittle and fragile, and subsequently carbon fiber was chosen.

Settling on carbon fiber composition, the design process turned to the architecture of the frame itself. The envisioned concept was one in which the dimensions of the frame allowed the encasement of the envelope without the need for direct attachment to the blimp. The concept required the frame to be designed such that the inflated envelope would expand against it and prevent the envelope from shifting position with respect to the frame. It was decided that two surrounding sections be connected by adjoining rods and dimensionally constructed to conform to the shape of the envelope. Discarding the

concept of rectangular surrounding sections in response to weight mitigation, the settled-

on approach was to form the surrounding sections as hexagons that conformed

dimensionally in height to the envelope and were held together by adjoining rods fixed at

the four lower vertices. Based on height and width measurements of the inflated

envelope, a rudimentary design for the surrounding hexagons was dimensionally

formulated and is illustrated in Figure 24, which shows a head-on view.
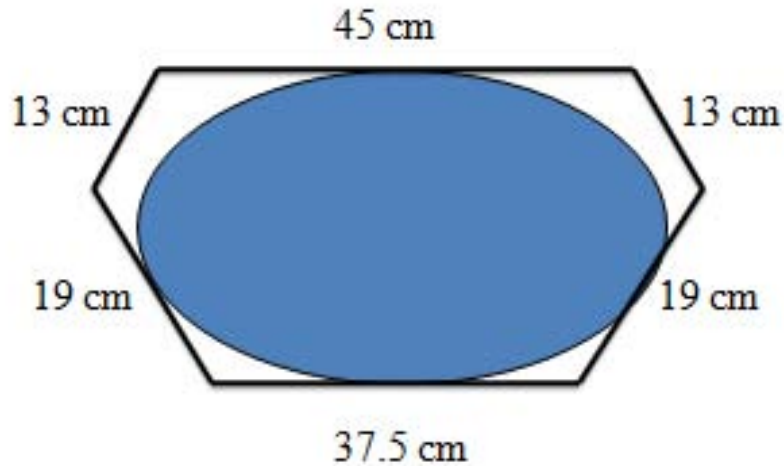
Figure 24. Rudimentary Design of Support Frame

The angle of the lower vertices was 120 degrees each, the mid vertices measured about

124 degrees each, and the upper vertices measured about 116 degrees each. Each section

was constructed from carbon tubing weighing 0.04561 grams per centimeter and having

an outside diameter of 0.098 inches and a 0.059 inch inside diameter.

Construction of each surrounding section began with cutting the carbon tubing, using a Dremel equipped with a Number 420 Cut-Off Wheel, into the appropriate lengths as annotated in Figure 24. It was then realized that a method of joining the tubing at the vertices had to be devised. Initial attempts were made by applying JB Weld to the tubing ends. The adhesive alone did not provide much strength to the joints and proved nonreliant as did attempts to affix the ends with solder. A viable approach was subsequently devised in which a 1.5 centimeter section of paperclip was cut, bent 120 degrees at the midpoint, coated with JB Weld, and each end inserted into the carbon tubing forming the angle. The upper portion of Figure 25 shows the setup before the JB Weld application, and the lower portion shows the completed joint.
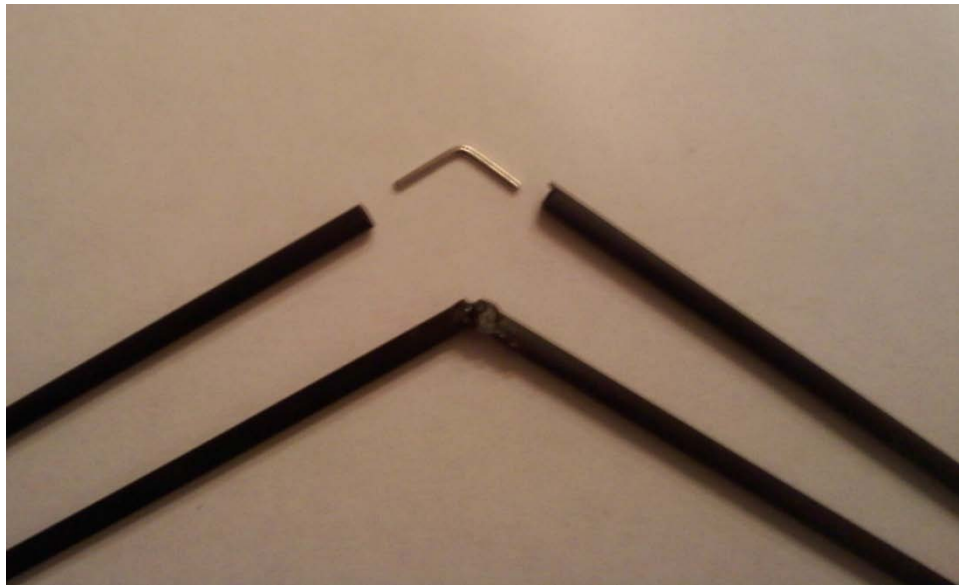
Figure 25. Tubing Attachment

After completing the hexagons, focus shifted to integrating the actuator components with the frame. A simplistic system, depicted in Figure 26, was conceived in which the contracting Nitinol wire would simultaneously pull two bellcranks. Each bellcrank would be attached to a pushrod serving as the physical means to impart force on a third-class lever action wing.
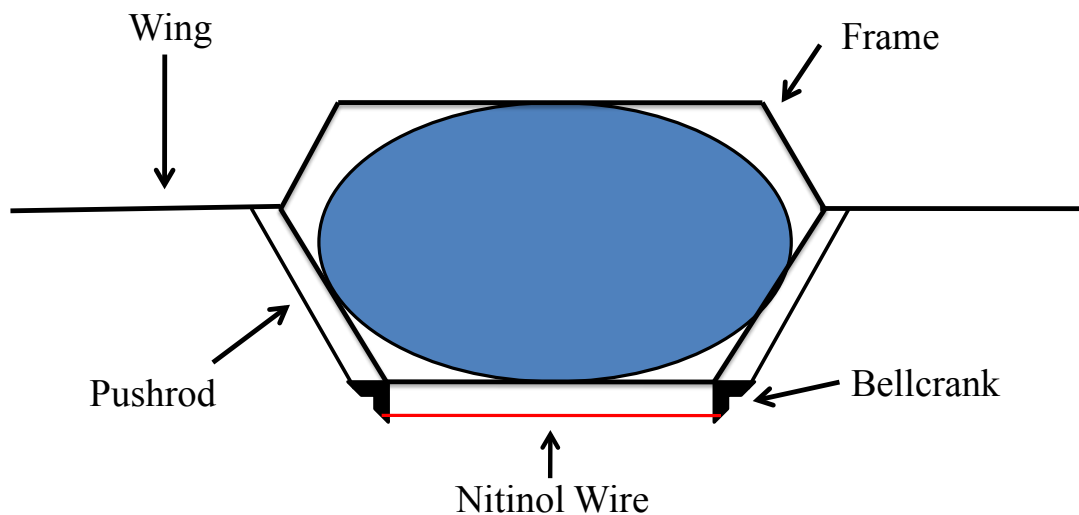
Figure 26. Prototype System

Components of the actuation system included two Du-Bro 90 degree micro bellcranks with mass of 0.158 grams each, two Du-Bro nylon kwik-link clevises with mass of 0.303 grams each, four Great Planes nylon swivel clevises with mass of 0.456 grams each, and two carbon fiber pushrods cut to 15 cm each. The carbon fiber pushrods were distributed by Midwest Products, had a diameter of 0.08 inches, and had a mass of 0.0472 grams per

centimeter. Figures 27, 28, and 29 depict the bellcrank, the nylon kwik-link clevis, and the nylon swivel clevis respectively.

Figure 27. Micro Bellcrank
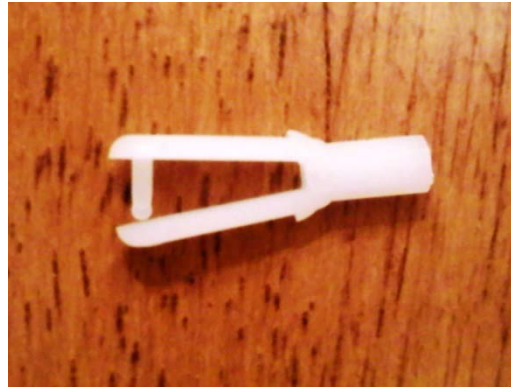
Figure 28. Kwik-link Clevis
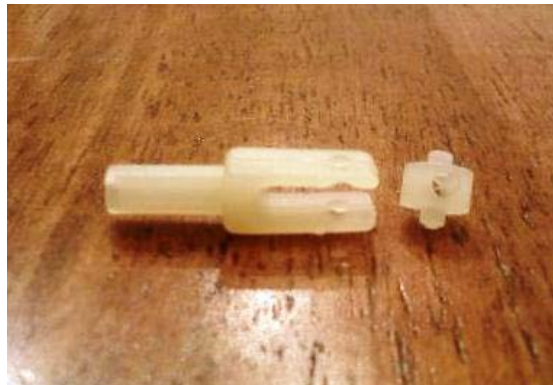
Figure 29. Swivel Clevis

The bellcranks were positioned on the ends of two carbon tubes measuring 8 cm each. The brass fitting of the bellcrank fit snuggly on the inserted carbon tubing and required no adhesive. With the brass fitting secure, the plastic portion of the belcrank was free to rotate about it. In addition to supporting the bellcrank, the carbon tubing would serve to

join the hexagons at the corresponding lower two vertices. Behind the bellcrank, a small plastic spacer was placed to prevent contact with the frame once the carbon tube was positioned. The interior angles of the hexagons' lower vertices were coated with JB Weld and the carbon tubes fitted with the bellcranks were positioned into the interior angles. The linkage between the pushrod and the bellcrank was made by a Kwik-Link clevis. One of the 15 cm pushrods was coated with JB Weld on one end, fitted to the clevis, and the clevis was then snapped into place through the lower hole on the arm of the bellcrank. Figure 30 shows a carbon tube, fitted with a bellcrank and spacer, fixed in position at the corresponding lower vertices of the two hexagons, and Figure 31 shows a head on view. Figure 32 shows the pushrod linked to the bellcrank via a Kwik-Link clevis.

Figure 30. Bellcrank Side View   **Figure 31.** Bellcrank Front View

Figure 32. Pushrod/Bellcrank Linkage

Once the pushrod and bellcrank linkages were complete, fabrication of the third-class lever system began. The lever system would function as the wing flapping mechanism. Similar to the bellcrank attachment, one of the swivel clevices was fitted to the end of a carbon tube, and the carbon tube fixed between the corresponding middle vertices of the two hexagons. In order to fit the swivel clevis to the spanning carbon tube, a 3/32 inch hole was drilled through the mid-section of the swivel clevis. The end of the carbon tube was coated with JB Weld and inserted through the hole. Finally, the carbon tube was fixed between the corresponding mid-point vertices of the hexagons with JB Weld. Figures 33 and 34 show the side view and front view of the resulting work.
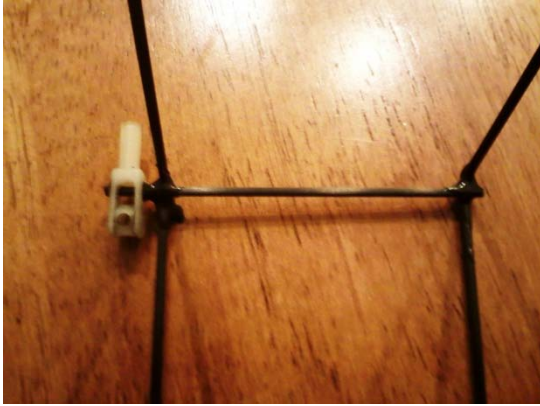
Figure 33. Swivel Attachment Side View

Figure 34. Swivel Attachment Front View

The ends of the pushrods opposite of the bellcrank linkages were coated with JB Weld and inserted into the ends of additional swivel clevises. One-foot sections of carbon tubing representing wings were inserted through the swivel holes of the frame-attached swivel clevises and the pushrod-attached swivel clevis. The carbon tubing was set in place with JB Weld in each of the swivel holes. A 1.5 cm section of pushrod was cut and fitted to the end of the frame-attached swivel clevis with JB Weld. This 1.5 cm section served as an anchor point for a bias spring, the other end of the spring fixed to the wing. The bias springs were included for use in a previously purchased Flexinol^{Tm} kit that contained the same diameter wires as the specimens investigated during this project. Because the spring constant and frictional forces between the components were unknown, the force required to impart motion on the third-class lever could not be calculated. The prototype would be configured and tested with each specimen individually to determine if adequate force could be generated to cause motion. Figure 35 shows the completed lever action mechanism. Figure 36 shows the completed frame and actuation system.
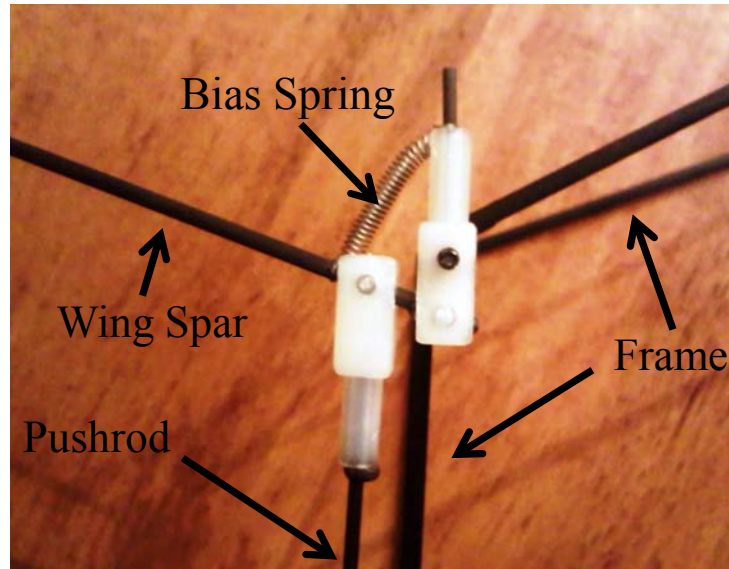
Figure 35. Lever Action System

Figure 36. Prototype Frame and Actuation System

Actuator Wire Preparation and Testing

The subsequent phase of the project involved preparing and testing specimen

Nitinol wires in conjunction with the fabricated actuation system. From each of the five

sizes of Nitinol wire, 38 centimeter length specimens were cut. To help ensure a

specimen wire would pull each bellcrank synchronously and that the magnitude of

motion would be equal for each bellcrank, the midsection of the wire had to be fixed with

respect to the frame. For each specimen wire, a 1.5 centimeter length of hypodermic

tubing was cut, the wire threaded through the tubing, and the tubing crimped at the

midpoint of the wire length. The wire was then threaded through a 22-16 gauge butt

splice until the hypodermic tubing was centered in the splice. With the splice in place, it

was then crimped to the tubing at midpoint. This arrangement provided a means to fix

the midpoint of the wire to the frame by clamping the splice to the frame. Terminal

points were fabricated on the ends of each wire specimen to be used as linkages to each

bellcrank. These terminal ends were fabricated from the same stainless-steel hypodermic

tubing used in the wire testing phase, the terminal points for the 0.0015, 0.002, and 0.003

specimens constructed from 26 gauge tubing and the terminal points for the 0.004, 0.005,

and 0.006 specimens constructed from the 22 gauge tubing. The process involved cutting

two sections, each measuring about 1.5 centimeters, of hypodermic tubing for each test

specimen and bending each section into a "V" shape with needle nose pliers. Each end of

the specimen wire was threaded into the "V" shaped hypodermic tubing until it stopped at

the vertex and then crimped in place. The ends of the terminals not crimped to the wire

were inserted into the lower holes of the bellcranks.

  With the specimens made, the actuation system was tested as a bench-top design

with each wire tested individually as a constituent of the system. The power arrangement

used in the wire kinematic testing phase provided the power during this testing phase, and

the leads were initially attached to the terminal points of the wire. The power arrangement limited voltage across the leads to 5 volts, and thus the ideal voltage for the given length of each specimen wire could not be attained. The leads were then placed at increasingly closer distances from the midpoint of the wire until the magnitude of wing motion reached its zenith, and motion was observed at increasing frequencies. Though this method was not ideal, visual observations determined which specimens could produce enough force to induce motion and provided a semblance of performance with respect to the magnitude of motion versus frequency.

IV. Analysis and Results

Wire Stroke Length

During the initial phase of the project, specimen wires were subjected to a cyclic voltage in order to determine stroke lengths for given cycling frequencies. This process utilized a laser vibrometer and SignalCalc 620 software to capture 2048 sample velocities over a selected time interval. The software only allowed the selection of predefined time intervals, and the selected value was chosen to correspond with the period of motion as precisely as possible. The process was repeated ten times for each frequency in order to statistically determine the percent strain expected for each wire as related to a given frequency. The initial Matlab code in Appendix A, used to calculate stroke length, assumed each sample block, consisting of 2048 velocity samples, represented exactly one cycle. While this would have been ideal, the software's predefined time intervals did not always correspond exactly with the period of motion, and thus some time block samples represented intervals slightly greater than one cycle. Additionally, some of these time block samples of greater than one cycle interval contained initial data points exceeding the zero-slope maxima and minima of the displacement curve representing the single cycle. These initial data points were attributed to preceding cycles of larger stroke length, and an example is shown in the displacement plot of Figure 37.
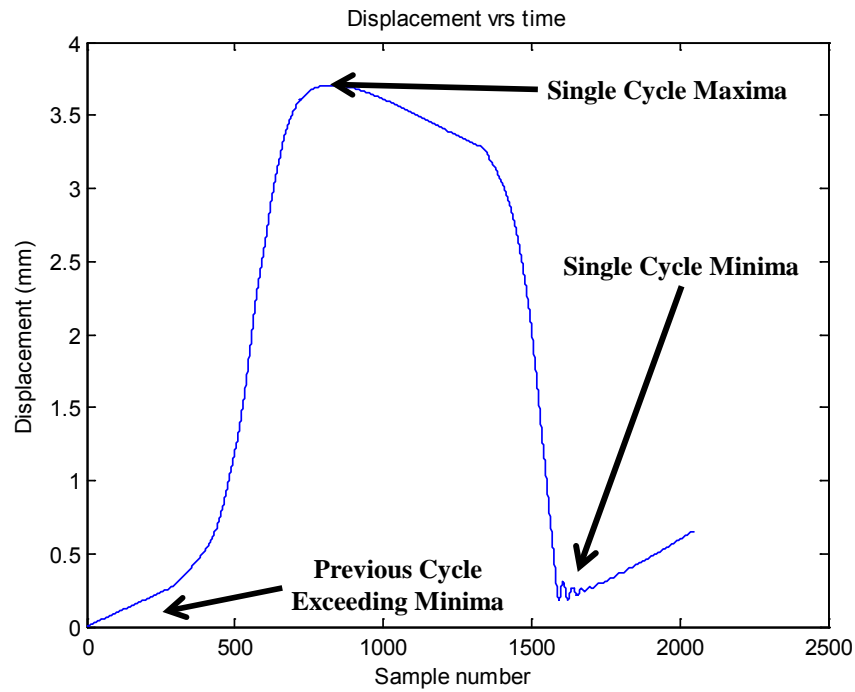
Figure 37. Previous Cycle Influence

It was determined that refinement of the original Matlab code was necessary to negate the influence of preceding cycles and ensure displacement calculations were made between zero-slope maxima and minima of the displacement curve. This refinement, as seen in the updated Matlab code of Appendix B, involved the introduction of a variable (n) which would define the first sampling point of the 2048 to be used in code calculations. For samples that displayed initial values exceeding the zero-slope maxima or minima, the value of the variable "n" was selected to define the first sample point of the domain over which displacement would be calculated, thereby negating the influence of the initial values. For example given the sampling data in Figure 37, the value of "n" would be set

50

to 500. The Matlab code would then discard samples 1 through 499, and the

displacement calculation would be made between samples 500 and 2048.

The first wire tested was the 100 millimeter long, 0.006 inch diameter specimen,

and it was subjected to a 300 gram bias mass as discussed in Section III. Calculations

presented in Table 4 of the Methodology section resulted in an ideal voltage of 2.04 volts

for the specimen. However, an exact voltage could not be set due to variance in the

power output, and the applied voltage was about 2.04 +/- 0.05volts. Appendix C lists the

ten resulting displacement measurements for each tested frequency. From the ten

displacement measurements, an average displacement was calculated for the frequency as

well as standard deviation and 95% confidence interval as listed in Table 5.

Table 5. 0.006 Inch Diameter Specimen Results

Frequency (Hz)	Average Displacement (mm)	Standard Deviation (mm)	95% Confidence (mm)
0.1	4.71941	0.51219	+/- 0.31746
0.2	2.49454	0.32715	+/- 0.20276
0.3	0.78697	0.35288	+/- 0.21871
0.4	0.20463	0.03316	+/- 0.02055
0.5	0.11133	0.01984	+/- 0.01230

The results in Table 5 show a rapidly decreasing average displacement with increasing

frequency. Ostensibly, the rapid decrease is attributed to the large mass to surface area

ratio resulting in a low cooling rate, and this decrease is best illustrated in Figure 38.

Because the length of the specimen was 100 millimeters, each average displacement also

translates to a percent strain that can be used to calculate expected strain in wires of

differing lengths. The standard deviations and 95% confidence levels provide a degree of

certainty in the consistency of motion

Displacement Versus Frequency
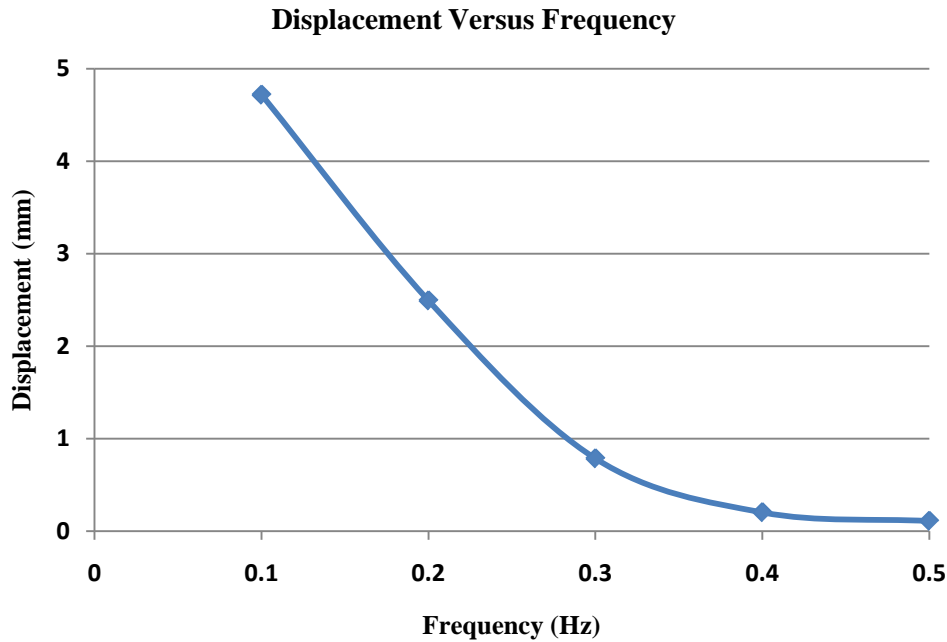
Figure 38. 0.006 Inch Diameter Wire Displacement Versus Frequency

The 0.005 inch diameter specimen wire was subjected to a 200 gram bias mass as

discussed in Section III. Calculations presented in Table 4 of the Methodology section

resulted in an ideal voltage of 1.77 volts for the specimen. As before, an exact voltage

could not be set due to variance in the power output, and the applied voltage was about

1.77 +/- 0.05volts. Appendix D lists the ten resulting displacement measurements for

each tested frequency. From the ten displacement measurements, an average

displacement was calculated for the frequency as well as standard deviation and 95%

confidence interval as listed in Table 6. Figure 39 displays the plot of the average

displacement versus frequency.

Table 6. 0.005 Inch Diameter Specimen Results

Frequency (Hz)	Average Displacement (mm)	Standard Deviation (mm)	95% Confidence (mm)
0.1	5.24167	0.10906	+/- 0.06759
0.2	4.05559	0.18457	+/- 0.11439
0.3	3.19086	0.26277	+/- 0.16286
0.4	2.18075	0.33353	+/- 0.20672
0.5	1.52558	0.38569	+/- 0.23905
0.6	0.83350	0.25097	+/- 0.15555
0.7	0.63352	0.16387	+/- 0.10157
0.8	0.44820	0.11017	+/- 0.06828
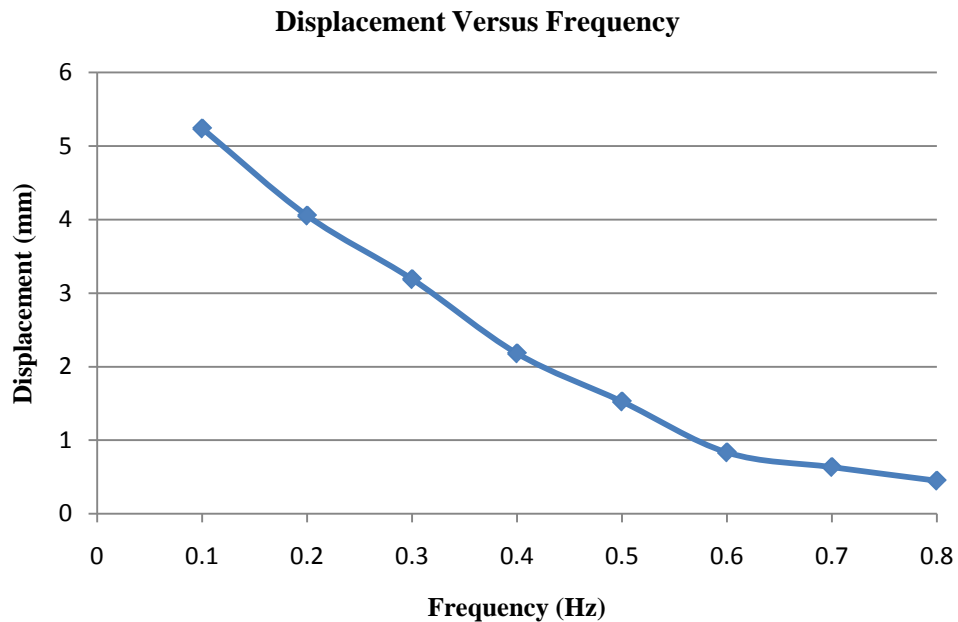
Figure 39. 0.005 Inch Diameter Wire Displacement Versus Frequency

As seen above, the displacement decreases at a lower rate versus frequency for the 0.005 inch diameter specimen compared to the 0.006 inch diameter specimen due to the smaller mass to surface area ratio.

The 0.004 inch diameter specimen wire was subjected to a 150 gram bias mass as discussed in Section III. Calculations presented in Table 4 of the Methodology section resulted in an ideal voltage of 2.12 volts for the specimen. As before, an exact voltage could not be set due to variance in the power output, and the applied voltage was about 2.12 +/- 0.05volts. Appendix E lists the ten resulting displacement measurements for each tested frequency. From the ten displacement measurements, an average displacement was calculated for the frequency as well as standard deviation and 95% confidence interval as listed in Table 7. Figure 40 displays the plot of the average displacement versus frequency.

Table 7. 0.004 Inch Diameter Specimen Results

Frequency (Hz)	Average Displacement (mm)	Standard Deviation (mm)	95% Confidence (mm)
0.1	5.29117	0.26403	+/- 0.16364
0.2	4.06367	0.10421	+/- 0.06459
0.3	3.67662	0.22602	+/- 0.14009
0.4	3.32311	0.14493	+/- 0.08983
0.5	3.21630	0.15939	+/- 0.09879
0.6	3.10949	0.11302	+/- 0.07005
0.7	2.69061	0.18024	+/- 0.11171
0.8	2.44508	0.30820	+/- 0.19102
0.9	2.21404	0.36868	+/- 0.22851
1.0	1.68472	0.47348	+/- 0.29346
1.1	1.68114	0.44551	+/- 0.27613
1.2	1.32669	0.32922	+/- 0.20405
1.3	1.12944	0.30884	+/- 0.19142
1.4	0.92361	0.18599	+/- 0.11528
1.5	0.78439	0.18495	+/- 0.11463
1.6	0.69673	0.23579	+/- 0.14614
1.7	0.56931	0.18779	+/- 0.11639
1.8	0.55288	0.19234	+/- 0.11921
1.9	0.58670	0.21268	+/- 0.13182
2.0	0.49067	0.10490	+/- 0.06502
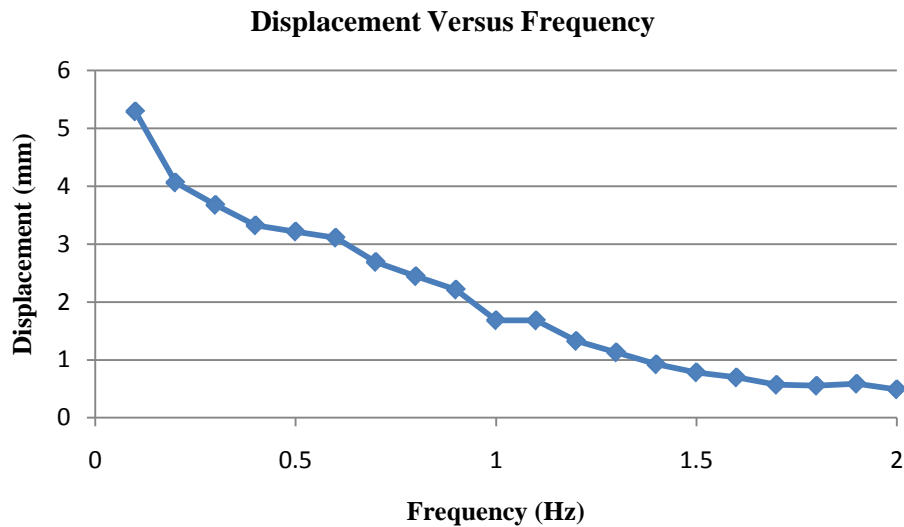
Figure 40. 0.004 Inch Diameter Wire Displacement Versus Frequency

The 0.003 inch diameter specimen wire was subjected to a 75 gram bias mass as discussed in Section III. Calculations presented in Table 4 of the Methodology section resulted in an ideal voltage of 1.96 volts for the specimen; however, the wire produced no visually observed movement at this voltage in contrast with visually evident displacements of the 0.006, 0.005, and 0.004 inch diameter wires. The voltage was increased until displacement at 0.1 hertz was visually evident and appeared to be at a maximum. This resulted in an applied voltage of 2.50 +/- 0.05 volts.   Appendix F lists the ten resulting displacement measurements for each tested frequency. From the ten displacement measurements, an average displacement was calculated for the frequency as well as standard deviation and 95% confidence interval as listed in Table 8. Figure 41 displays the plot of the average displacement versus frequency.

Table 8. 0.003 Inch Diameter Specimen Results

Frequency (Hz)	Average Displacement (mm)	Standard Deviation (mm)	95% Confidence (mm)
0.1	5.63374	0.32271	+/- 0.20001
0.2	4.47232	0.30046	+/- 0.18623
0.3	3.94643	0.30107	+/- 0.18660
0.4	3.61870	0.23111	+/- 0.14324
0.5	3.52150	0.22983	+/- 0.14245
0.6	3.19926	0.19519	+/- 0.12098
0.7	3.05384	0.19341	+/- 0.11988
0.8	3.07014	0.11428	+/- 0.07083
0.9	2.74913	0.34210	+/- 0.21203
1.0	2.89821	0.19310	+/- 0.11968
1.1	2.65286	0.25922	+/- 0.16067
1.2	2.21470	0.58294	+/- 0.36131
1.3	2.38849	0.38408	+/- 0.23805
1.4	2.18967	0.46097	+/- 0.28571
1.5	2.22352	0.27017	+/- 0.16745
1.6	1.55351	0.57245	+/- 0.35480
1.7	1.33280	0.44887	+/- 0.27821
1.8	1.24272	0.33757	+/- 0.20922
1.9	1.23969	0.49190	+/- 0.30488
2.0	0.84844	0.22308	+/- 0.13827
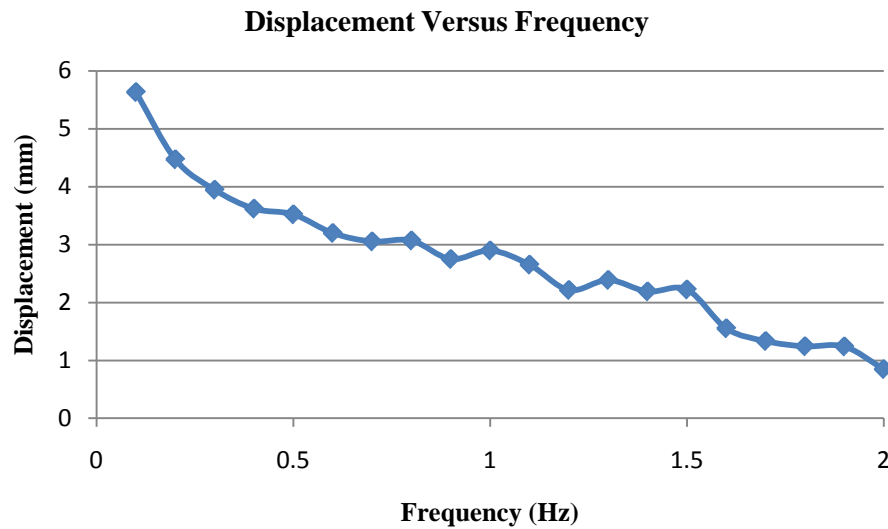
Figure 41. 0.003 Inch Diameter Wire Displacement Versus Frequency

The 0.002 inch diameter specimen wire was subjected to a 20 gram bias mass as discussed in Section III. Calculations presented in Table 4 of the Methodology section resulted in an ideal voltage of 2.36 volts for the specimen; however, the wire produced no visually observed movement at this voltage. The voltage was increased until displacement at 0.1 hertz was visually evident and appeared to be at a maximum. This resulted in an applied voltage of 3.00 +/- 0.05 volts. Appendix G lists the ten resulting displacement measurements for each tested frequency. From the ten displacement measurements, an average displacement was calculated for the frequency as well as standard deviation and 95% confidence interval as listed in Table 9. Figure 42 displays the plot of the average displacement versus frequency.

Table 9. 0.002 Inch Diameter Specimen Results

| Frequency (Hz)	Average Displacement (mm)	Standard Deviation (mm)	95% Confidence (mm)
0.1	6.07380	0.15119	+/- 0.09371
0.2	4.96833	0.12424	+/- 0.07700
0.3	4.48524	0.09719	+/- 0.06024
0.4	4.25226	0.05895	+/- 0.03654
0.5	3.69114	0.09670	+/- 0.05993
0.6	3.55844	0.05572	+/- 0.03454
0.7	3.47558	0.03175	+/- 0.01968
0.8	3.45849	0.05131	+/- 0.03180
0.9	3.28169	0.11906	+/- 0.07379
1.0	3.18518	0.12629	+/- 0.07827
1.1	3.13330	0.10854	+/- 0.06727
1.2	2.84933	0.49478	+/- 0.30666
1.3	2.78288	0.19025	+/- 0.11791
1.4	2.21507	0.49785	+/- 0.30857
1.5	1.80908	0.47193	+/- 0.29250
1.6	1.93150	0.64515	+/- 0.39986
1.7	2.22615	0.75006	+/- 0.46489
1.8	1.88090	0.60092	+/- 0.37244
1.9	1.77979	0.41140	+/- 0.25498
2.0	1.33755	0.33422	+/- 0.20715
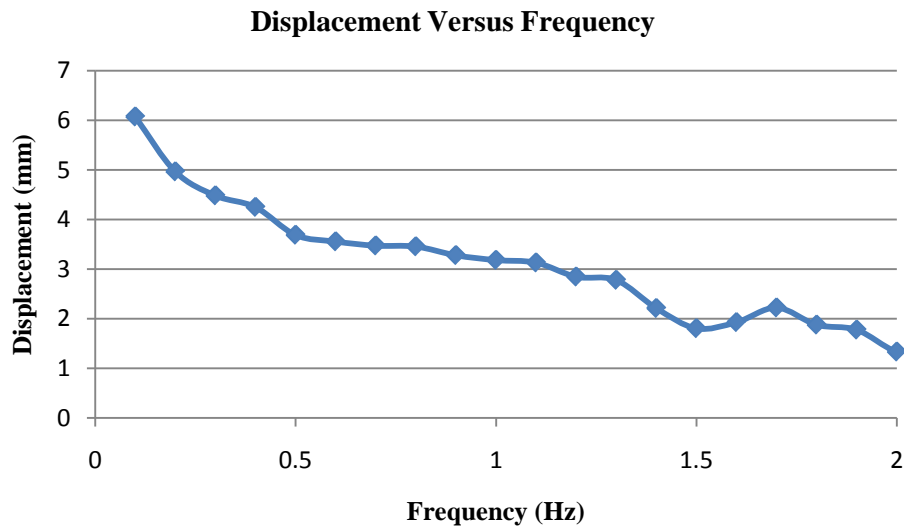
Figure 42. 0.002 Inch Diameter Wire Displacement Versus Frequency

The 0.0015 inch diameter specimen wire was subjected to a 10 gram bias mass as discussed in Section III. Calculations presented in Table 4 of the Methodology section resulted in an ideal voltage of 2.48 volts for the specimen; however, the wire produced no visually observed movement at this voltage. The voltage was increased until displacement at 0.1 hertz was visually evident and appeared to be at a maximum. This resulted in an applied voltage of 4.00 +/- 0.05 volts. Appendix H lists the ten resulting displacement measurements for each tested frequency. From the ten displacement measurements, an average displacement was calculated for the frequency as well as standard deviation and 95% confidence interval as listed in Table 10. Figure 43 displays the plot of the average displacement versus frequency. Additionally, Figure 44 is an aggregate plot of displacement versus frequency for each wire.

Table 10. 0.0015 Inch Diameter Specimen Results

Frequency (Hz)	Average Displacement (mm)	Standard Deviation (mm)	95% Confidence (mm)
0.1	4.64361	0.44402	+/- 0.27520
0.2	3.64253	0.52924	+/- 0.32802
0.3	2.94705	0.37194	+/- 0.23053
0.4	2.81282	0.36184	+/- 0.22427
0.5	2.79868	0.21131	+/- 0.13097
0.6	2.74071	0.22512	+/- 0.13953
0.7	2.82888	0.19201	+/- 0.11901
0.8	2.82278	0.19549	+/- 0.12117
0.9	2.81839	0.12840	+/- 0.07958
1.0	2.66584	0.18110	+/- 0.11225
1.1	2.79358	0.22402	+/- 0.13885
1.2	2.80575	0.13162	+/- 0.08158
1.3	2.78034	0.28630	+/- 0.17745
1.4	2.68136	0.26716	+/- 0.16559
1.5	2.65815	0.13578	+/- 0.08415
1.6	2.71539	0.06098	+/- 0.03779
1.7	2.52334	0.24146	+/- 0.14966
1.8	2.45340	0.14366	+/- 0.08904
1.9	2.34208	0.09932	+/- 0.06156
2.0	2.10643	0.30654	+/- 0.18999
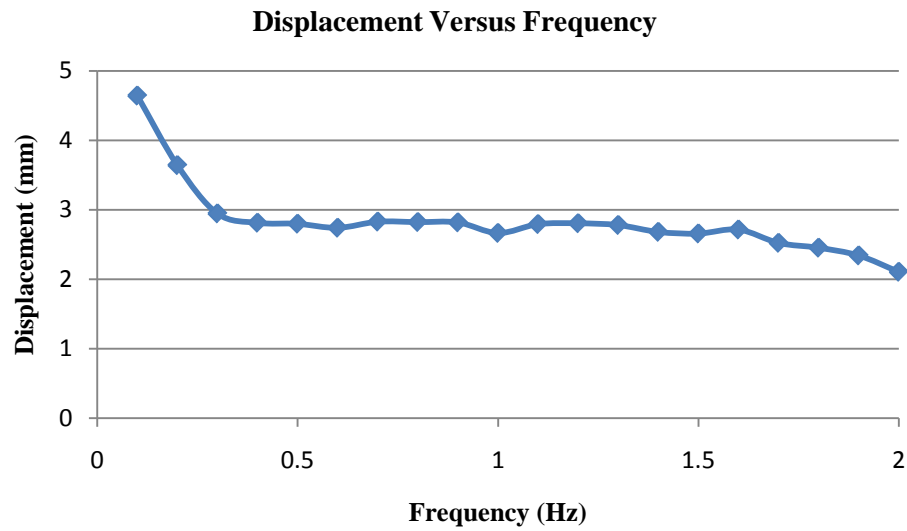
Figure 43. 0.0015 Inch Diameter Wire Displacement Versus Frequency
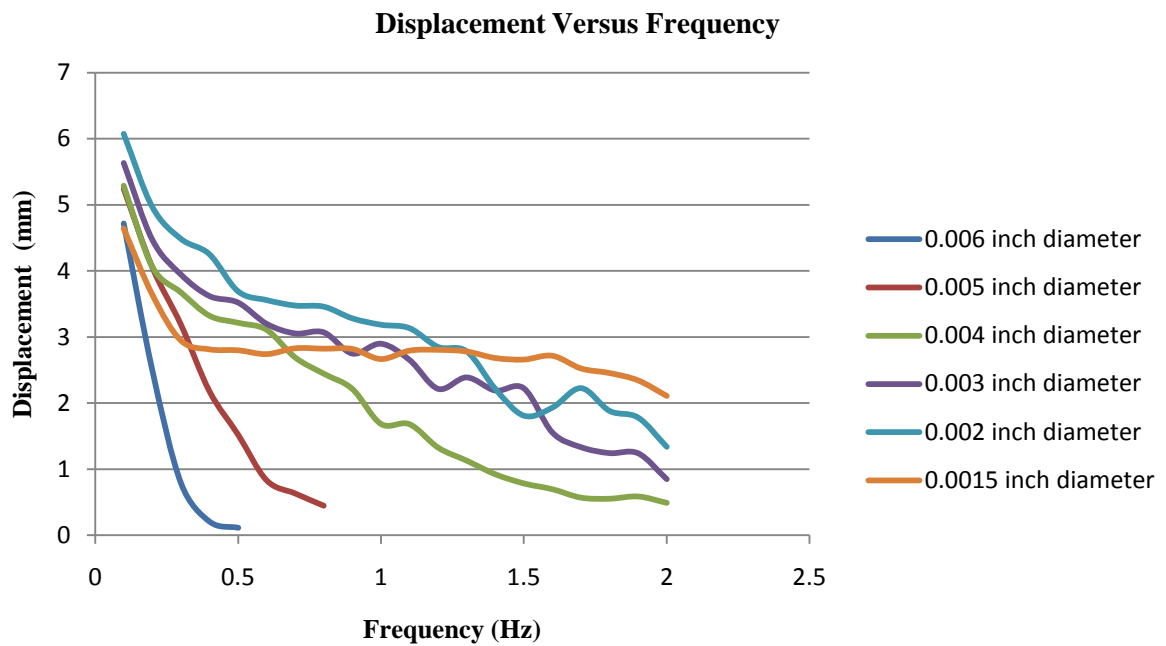
Figure 44. Aggregate Results

60

Analysis of the collected data reveals an inverse relationship between cycling frequency and stroke length. As frequency was increased, the duration of the cycle's power-off phase decreased. The decreased duration of the power-off phase resulted in less time for the specimen to dissipate heat between power applications. The martensite start temperatures of the specimens were reached during the power-off phases of each tested frequency as evident in the specimens' elongations, however minute. As frequency was increased, the fully martensitic state corresponding to full elongation could not be reached during the power-off phase because the cooling rate was not great enough for the specimens to attain the martensite finish temperature. The temperature of the specimens resided between the martensite start and finish temperatures at the end of each power-off phase. The realized specimen temperature at the end of each power-off phase resulted in fractional martensitic composition as generalized in Figure 8 of Section II, and equated to a shorter elongation as generalized in Figure 10 of the same section. Thus, the realized temperature at the end of each power-off phase was higher, the martensitic fraction lower, and the elongation shorter for each increase in frequency. Additionally, the slopes presented in Figure 44 reveal the effect of the surface area to mass ratio. Wires with larger diameters, reflecting greater surface area to mass ratios, produce more pronounced slopes than those of smaller diameter due to their slower rates of cooling.

In light of this analysis, the selection of wire diameter to actuate a flapping wing device is constrained by the scale of the design. As the scale of a design is decreased, it becomes necessary to select wires of smaller diameter to achieve the greater required

flapping frequencies. Additionally, methods to increase the cooling rate may be required to retain functional displacements.

Prototype Response

After quantifying the kinematics of the specimen wires, the project's focus shifted to determining the prototype's functional response while incorporating each sized wire. The results presented in the previous section provided foundational data upon which the cursory selection of wire could be made. As evident from the data, smaller wire diameter was necessary to produce beneficial displacements at higher frequencies. The displacement generated by the wire translated to the magnitude of the flapping motion, defined as the angular wing displacement as shown in Figure 45, while the flapping rate equaled the frequency setting.
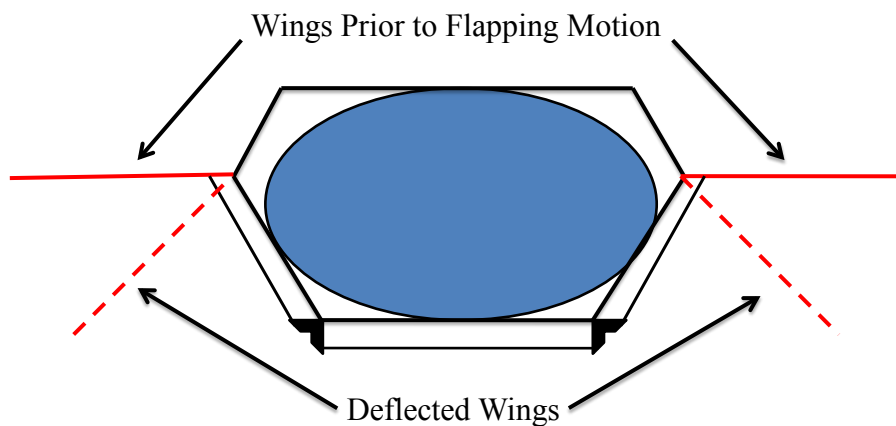
Figure 45. Flapping Motion Depiction

An additional constraint governing performance was the maximum pull force of the wire as cited in Table 2. While smaller diameter wires are capable of imparting larger displacements at higher frequencies, the pull force of these contractions decreases greatly with decreasing wire diameter. When individually incorporating the 0.0015, 0.002, and 0.003 inch diameter wires, the prototype displayed no motion. No motion was observed for these specimens regardless of where the leads were placed along the wire, and it was concluded that the specimens could not produce enough pull force to impart a torque on the third-class lever system as designed. Integration of the 0.006 inch diameter wire with the prototype resulted in 40 to 50 degrees of flapping motion at 0.1 Hz with the leads placed about 25 centimeters apart. Increasing the frequency to 0.2 Hz resulted in about 10 to 15 degrees of motion. The decreased range of motion was consistent with the results of the specimen wire testing phase presented in the first part of Section IV. This decreased range of motion is traced to the inadequate cooling rate with respect to the frequency as previously discussed. The specimen was heated to the fully austenite state with power application. However, during the time interval in which the power was cycled off, the specimen could not dissipate enough latent heat to reach the martensite finish temperature, and thus complete elongation associated with a fully martensite specimen could not be realized. Incorporation of the 0.005 inch diameter wire produced about 40-50 degrees of movement at 0.1 and 0.2 Hz with the leads positioned about 20 centimeters apart. Increasing the frequency to 0.3 Hz resulted in about 15 to 20 degrees of movement. Finally, the 0.004 inch diameter wire produced about 40-50 degrees of movement at 0.1 and 0.2 Hz with the leads positioned about 25 centimeters apart. A

frequency of 0.3 Hz resulted in about 30 to 40 degrees of movement, and 0.4 Hz resulted

in movement of 25 to 35 degrees.

Based on the bench-top performance, a circuit was constructed by Air Force

Institute of Technology lab technician Sean Miller for the flying prototype. The circuit

provided cycling voltage at a frequency of 0.2 Hz, reflecting the bench-top frequency that

resulted in 40-50 degrees of movement for the 0.004 and 0.005 inch diameter specimens.

Additionally, the circuit had a mass of 10.5 grams, and Figure 46 is a schematic of the

circuit.
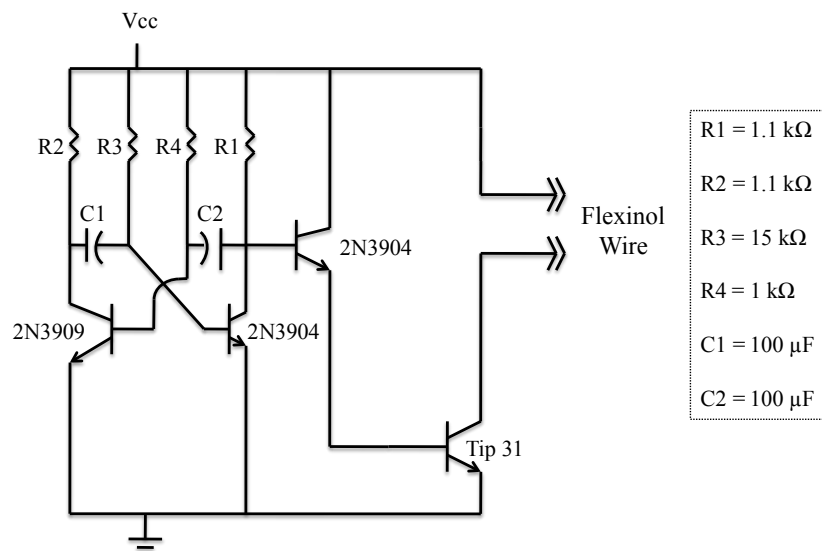
Figure 46. Flying Prototype Circuit

System Refinement

With bench-top observations complete, the blimp envelope was encased by the

prototype to determine whether the prototype conformed to the weight restrictions of the

buoyant force. It was determined that the weight of the prototype frame and actuation

system surpassed the buoyant force. Additional observation revealed that the prototype

frame was dimensionally larger than necessary. The envelope did not provide a

substantive reference frame from which to determine accurate angles and dimensions

when designing the prototype frame. With the prototype frame encasing the envelope,

more exacting dimensional measurements for a subsequent design were determined and

are detailed in Figure 47.
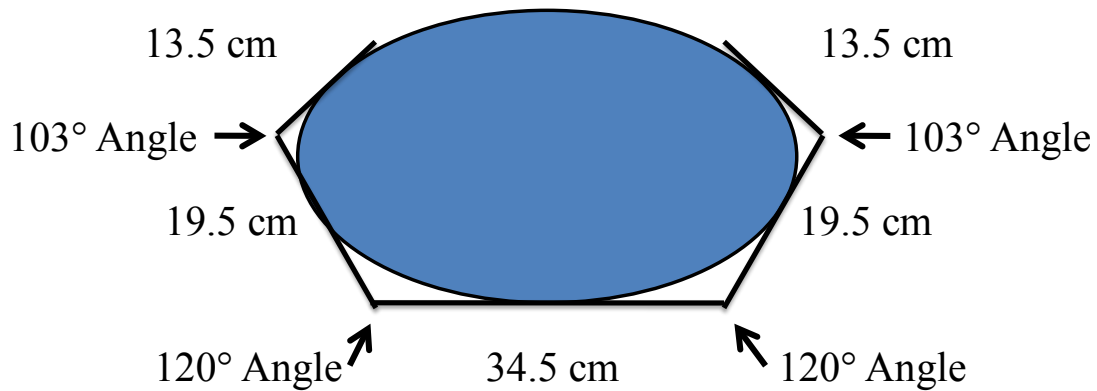
Figure 47. Mod-2 Dimensions

The more precise dimensions reduced the total length of required tubing, thus decreasing

the gross weight of the frame. The modified design did not include the upper portion of

each hexagon, thereby further reducing the weight. Instead, the semi-hexagons were

joined at the upper termination points by 6.5 centimeter lengths of tubing, as were the

corresponding vertices. Additionally, the refined design was constructed with thinner

carbon tubing having an outer diameter of 0.080 inches, an inner diameter of 0.040

inches, and a weight of 0.03421 grams per centimeter. Fabrication of the joints and fitting of the actuator components were accomplished in the same manner as with the prototype construction detailed in Section III; however, powdered graphite lubricant was applied to the swivels of the swivel clevises to reduce friction. Before the pushrods and wings were fitted, the new structure weighed 13.2 grams, whereas the prototype weighed 16.5 grams in the same configuration. Figure 48 shows the completed structure before pushrod and wing fitting.
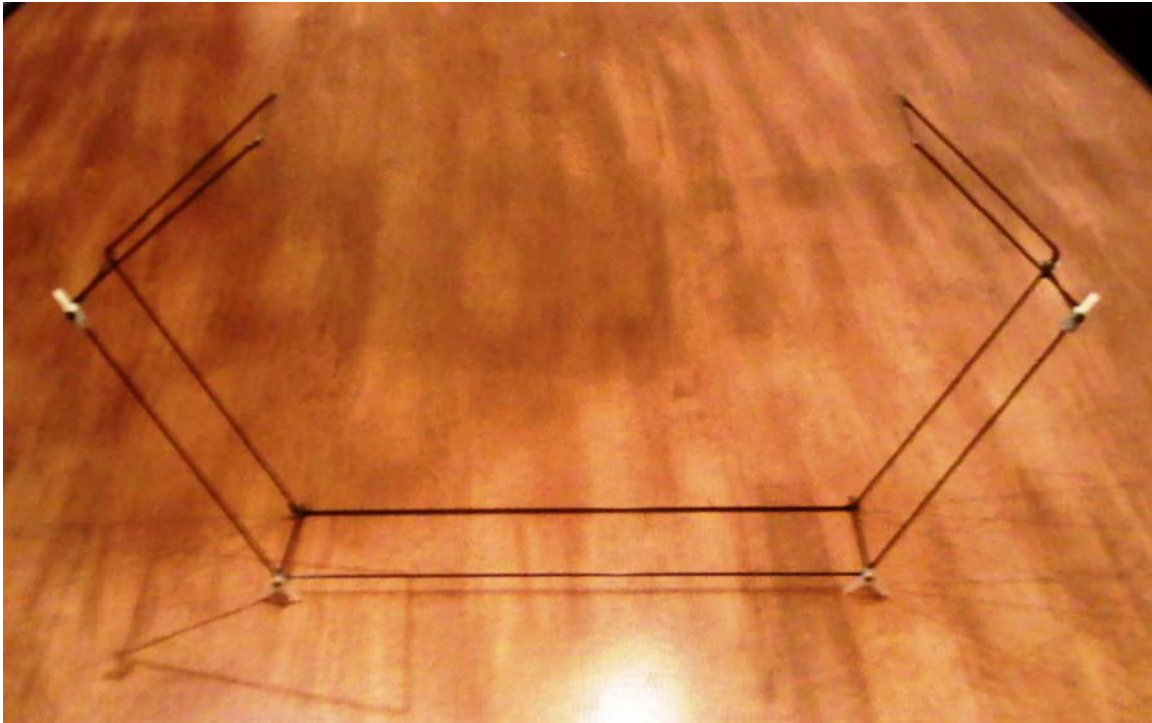
Figure 48. Mod-2 Frame

Wings were constructed with the same carbon tubing comprising the Mod-2 frame, and the joints fashioned by the same method as those in the frame. Figure 49

represents the frame dimensions of the wings which would be covered with mylar. The

design was simplistic because the focus of the project centered on the proof of concept

regarding shape memory alloy actuation and not optimal wing design. After constructing

this wing, the design was deemed incompatible with the actuator. The off-center design

would produce a torque about the wing root spar, which would break the root's adhesion

to the swivel clevises. A new wing design incorporated the 25.4 centimeter by 12.7

centimeter frame; however, the wing root spar was centrally fixed with JB weld as

depicted in Figure 50. Figure 51 shows the completed Mod-2 prototype.
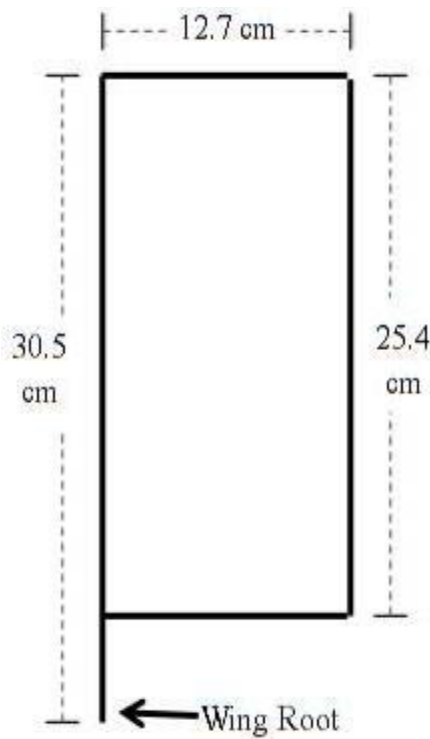
Figure 49. Initial Wing Design

Figure 50. Refined Wing Design
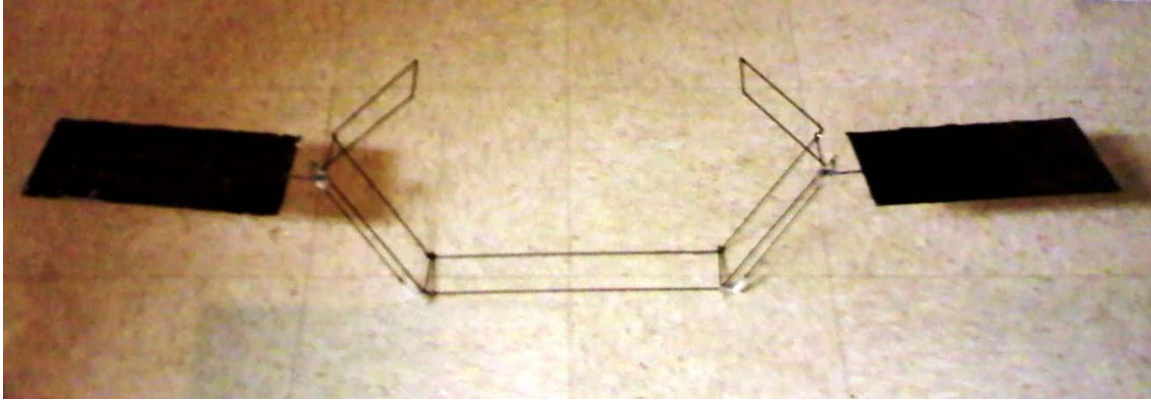
Figure 51. Completed Mod-2 Prototype

After wing attachments were made, the blimp envelope was encased with the

Mod-2 Prototype. Although the Mod-2 fit well with the envelope dimensions, the

envelope did not have enough buoyant force to levitate weight of the Mod-2 with the

attached wings. A larger envelope, capable of greater buoyancy, was purchased from the

same distributer as the original envelope. The larger envelope had the same shape as the

24 inch original, but was advertised as a 38 inch envelope. The Mod -2 was fitted to the

partially inflated 38 inch envelope, the shape of the envelope modified, and the envelope

filled to capacity with helium. Modification was accomplished by constricting the mid-

section with tape so the Mod-2 would not be damaged by further inflation. Thin ribbon,

tightly joining the top connecting rods of the frame, ensured the Mod-2 would stay in

place. Figure 52 depicts the top view of the Mod-2 fitted to the 38 inch envelope, and

Figure 53 shows a quartering shot of the tethered system.

Figure 52. Mod-2 Fitted to 38 Inch Envelope

Figure 53. Mod-2/Envelope Alternate View

Actuator wires were fabricated from 0.006, 0.005, 0.004, 0.003, 0.002, and 0.0015 inch diameter Flexinol^{TM} wire as described in Section III. The wires had masses of 0.0011, 0.0008, 0.00047, 0.00028, 0.00015, and 0.00012 grams per centimeter respectively. Their lengths were 34.3 centimeters to conform to the Mod-2 design. The

circuit represented in Figure 46 was used in conjunction with a Number 529, 6 volt Energizer battery to produce a 0.2 hertz cycling voltage across each actuator wire individually. Because the envelope could not levitate the additional 10.5 gram mass of the circuit, the circuit was placed on a table with the battery, and the leads were connected to the actuator wire of the tethered Mod-2 blimp. As with the prototype response previously chronicled in this section, the 0.003, 0.002, and 0.0015 inch diameter wires produced no flapping motion. Incorporation of the 0.004 inch diameter wire resulted in approximately 5 to 10 degrees of flapping motion with the leads spaced 27 centimeters apart. The decrease in angular deflection as compared to that produced in the original prototype by the 0.004 inch diameter wire was likely a result of the increased mass of the Mod-2's wings. An analogous decrease was witnessed in the motion produced by the 0.005 inch diameter wire. The deflection of the wings measured about 25 to 35 degrees when the leads were spaced about 20 centimeters along the 0.005 inch diameter wire, and proved to be the greatest of any wire. Finally, the 0.006 inch diameter wire deflected the wings about 5 degrees, attributable to the slow cooling rate of the specimen as discussed earlier in this section.

V. Conclusions and Recommendations

Conclusions of Research

While the focus of this project was a proof of concept regarding shape memory actuation of a flapping blimp, much information was garnered from the specimen wire testing and the vehicle design phases. Although shape memory alloys have significant weight advantages compared to rotational motors, their employment within an actuation system presents intricate challenges. Issues of resistance, voltage, current, specimen length, motion tolerance, force, and cooling rate must be managed effectively and simultaneously. To optimize a shape memory actuator, exact voltage must be applied based on the wire's length, diameter, and ideal current. The voltages of commercially available power supplies do not always correspond to the precise voltage requirements of a designed shape memory actuator, and higher or lower voltages result in permanent strain or decreased stroke length. Motion tolerances present another challenge to the design. Because of the fluctuations in temperature and airflow within the vicinity of the wire, cooling rate is continuously effected, and thus stroke length is not constant. Variations in stroke length were witnessed in the relatively constant setting of the lab. While no concrete trends of variation were discovered, as a generalization the confidence limits showed that differences in successive stroke lengths could be on the order of 10 percent. Additionally, wire performance must be weighed against the system's design in terms of required force, necessary frequency, and desired stroke length.

Designing a flapping blimp also presented valuable insight. While the carbon tubing frame provided support and structure for the actuation system, it consumed valuable weight that could be allotted to other components. Construction of the frame generated unique challenges and solutions regarding joint fabrication and actuator component integration. Furthermore, even though the actuation design was simple, it required exact symmetry of pushrod lengths, swivel clevis spacing, and linkage attachments to produce reflective motion of the wings. As a proof of concept, the system demonstrated the feasibility of a shape memory actuated flapping mechanism. While the demonstration was constrained by force requirements, size, and mechanism design, these variables can be tailored to optimize the performance of a shape memory actuated flapping mechanism.

Recommendations for Future Research

Recommendations for subsequent projects include the exploration of cooling techniques and the investigation of wing shaping by means of shape memory alloys. With regards to the former, development of a viable means to increase the cooling rate of a shape memory alloy wire would prove advantageous with respect to the attainable stroke length and range of motion at increasing frequencies. As for the latter, if shape memory alloy wires were configured and controlled in an analogous manner as the tendons and muscles of a bird's wings, biomimetic flight could be realized.

Appendix A. Initial Matlab Code

```matlab
% LCDR Jeffery Barrett
% Program to convert cyclic velocity of SMA to displacement

close all;
clc;

V=X2(:,2);
t=X2(:,1);
Vel=10*V;

Veladjust=Vel(1:2048);
tadjust=t(1:2048);
c=2048;

x(1)=0;
for k=[1:c];
    x(k+1)=trapz(tadjust(k:k+1),Veladjust(k:k+1))+x(k);
end

d=max(x)-min(x);

figure
plot(tadjust,Veladjust);
title('Velocity vrs time');
xlabel('Time (s)');
ylabel('Velocity (mm/s)');

figure
plot(x);
title('Displacement vrs time');
xlabel('Sample number ');
ylabel('Displacement (mm)');

clear x;
clear Veladjust;
clear tadjust;
clear V;
clear t;
clear Vel;
clear c;
clear d;
clear k;
clear n;
```

Appendix B. Refined Matlab Code

```matlab
% LCDR Jeffery Barrett
% Updated program to convert cyclic velocity of SMA to displacement

close all;
clc;

n=500;  % Shifts velocity data as necessary

V=X2(:,2);
t=X2(:,1);
Vel=10*V;

Veladjust=Vel(n:2048);  % Eliminating previous cycle influence
tadjust=t(n:2048);  % Shifting the time domain
c=(2048-n);

x(1)=0;
for k=[1:c]
    x(k+1)=trapz(tadjust(k:k+1),Veladjust(k:k+1))+x(k);
end

d=max(x)-min(x)

figure
plot(tadjust,Veladjust);
title('Velocity vrs time');
xlabel('Time (s)');
ylabel('Velocity (mm/s)');

figure
plot(x);
title('Displacement vrs time');
xlabel('Sample number ');
ylabel('Displacement (mm)');

clear x;
clear Veladjust;
clear tadjust;
clear V;
clear t;
clear Vel;
clear c;
clear d;
clear k;
clear n;
```

Appendix C. 0.006 Inch Diameter Wire Displacement Results

Frequency (Hz)	Displacement (mm)	Frequency (Hz)	Displacement (mm)
0.1	4.33819	0.4	0.23989
0.1	4.59604	0.4	0.15902
0.1	5.48754	0.4	0.19823
0.1	4.50442	0.4	0.20118
0.1	4.43375	0.4	0.23097
0.1	5.49376	0.4	0.22459
0.1	4.28832	0.4	0.14829
0.1	4.30627	0.4	0.18865
0.1	4.38330	0.4	0.24929
0.1	5.36251	0.4	0.20615
0.2	2.91243	0.5	0.10119
0.2	2.61680	0.5	0.09331
0.2	2.52139	0.5	0.12691
0.2	2.35241	0.5	0.12491
0.2	2.70784	0.5	0.11906
0.2	2.71207	0.5	0.11692
0.2	2.00729	0.5	0.12646
0.2	2.36611	0.5	0.13605
0.2	2.80887	0.5	0.09632
0.2	1.94028	0.5	0.07219
0.3	0.31745		
0.3	1.03508		
0.3	0.72522		
0.3	0.39523		
0.3	1.02133		
0.3	1.14040		
0.3	0.49097		
0.3	0.95828		
0.3	1.31844		
0.3	0.46732		

Appendix D.   0.005 Inch Diameter Wire Displacement Results

Frequency (Hz)	Displacement (mm)	Frequency (Hz)	Displacement (mm)
0.1	5.17354	0.4	2.35458
0.1	5.22884	0.4	2.56656
0.1	5.12305	0.4	2.29623
0.1	5.25921	0.4	2.00470
0.1	5.33681	0.4	1.74802
0.1	5.33980	0.4	1.57011
0.1	5.18948	0.4	2.19057
0.1	5.26808	0.4	2.35885
0.1	5.06777	0.4	2.11156
0.1	5.43013	0.4	2.60627
0.2	3.92815	0.5	2.02938
0.2	3.88199	0.5	1.65058
0.2	4.12139	0.5	1.98534
0.2	4.13185	0.5	1.32281
0.2	3.80910	0.5	1.97098
0.2	4.18137	0.5	1.09747
0.2	4.23597	0.5	1.11078
0.2	4.19886	0.5	1.47119
0.2	4.27799	0.5	1.02046
0.2	3.78920	0.5	1.59678
0.3	2.53392	0.6	0.40612
0.3	3.39730	0.6	0.47318
0.3	3.24161	0.6	0.79790
0.3	3.18832	0.6	0.97482
0.3	3.28222	0.6	1.01396
0.3	3.12970	0.6	1.05155
0.3	3.39040	0.6	0.79433
0.3	3.07936	0.6	0.69439
0.3	3.19146	0.6	1.17745
0.3	3.47426	0.6	0.95127

Frequency (Hz)	Displacement (mm)
0.7	0.48420
0.7	0.55102
0.7	0.67318
0.7	0.96073
0.7	0.50274
0.7	0.51283
0.7	0.79378
0.7	0.78875
0.7	0.57053
0.7	0.49742
0.8	0.31666
0.8	0.46802
0.8	0.61480
0.8	0.41339
0.8	0.34199
0.8	0.51599
0.8	0.63940
0.8	0.38040
0.8	0.39276
0.8	0.39859

Appendix E.   0.004 Inch Diameter Wire Displacement Results

Frequency (Hz)	Displacement (mm)	Frequency (Hz)	Displacement (mm)
0.1	5.18537	0.4	3.31545
0.1	5.54248	0.4	3.60371
0.1	5.58442	0.4	3.17139
0.1	5.11958	0.4	3.30439
0.1	5.00139	0.4	3.35156
0.1	5.15487	0.4	3.22055
0.1	5.63307	0.4	3.17798
0.1	5.08831	0.4	3.54228
0.1	5.59844	0.4	3.29647
0.1	5.00377	0.4	3.24731
0.2	4.12955	0.5	3.11998
0.2	4.08683	0.5	3.29105
0.2	4.15683	0.5	3.28486
0.2	4.19140	0.5	3.13037
0.2	3.99462	0.5	3.09337
0.2	3.94072	0.5	2.95513
0.2	3.92321	0.5	3.39841
0.2	4.06826	0.5	3.43256
0.2	4.20139	0.5	3.09057
0.2	3.94390	0.5	3.36674
0.3	3.86931	0.6	3.03379
0.3	3.43154	0.6	3.23345
0.3	3.66407	0.6	3.24660
0.3	3.49391	0.6	3.09194
0.3	3.98697	0.6	3.12454
0.3	3.87118	0.6	3.12503
0.3	3.56345	0.6	2.84039
0.3	3.96914	0.6	3.12162
0.3	3.43405	0.6	3.14144
0.3	3.48257	0.6	3.13614

Frequency (Hz)	Displacement (mm)	Frequency (Hz)	Displacement (mm)
0.7	2.48151	1.0	0.85784
0.7	2.44098	1.0	2.34016
0.7	2.75016	1.0	1.36049
0.7	2.70603	1.0	1.85793
0.7	3.07030	1.0	2.02222
0.7	2.84257	1.0	1.98655
0.7	2.65148	1.0	2.09693
0.7	2.64969	1.0	1.17206
0.7	2.72664	1.0	1.80892
0.7	2.58674	1.0	1.34408
0.8	2.00687	1.1	0.76116
0.8	2.54845	1.1	2.08449
0.8	2.04042	1.1	1.48636
0.8	2.87121	1.1	1.80606
0.8	2.17828	1.1	2.28415
0.8	2.64777	1.1	1.55231
0.8	2.66550	1.1	1.36407
0.8	2.62269	1.1	1.63949
0.8	2.67375	1.1	2.17190
0.8	2.19584	1.1	1.66139
0.9	2.64724	1.2	0.64661
0.9	1.99163	1.2	1.41027
0.9	2.07157	1.2	1.05275
0.9	1.33273	1.2	1.50254
0.9	2.22856	1.2	1.01242
0.9	2.20567	1.2	1.50172
0.9	2.38111	1.2	1.71827
0.9	2.53777	1.2	1.32933
0.9	2.42800	1.2	1.44490
0.9	2.31615	1.2	1.64806

Frequency (Hz)	Displacement (mm)	Frequency (Hz)	Displacement (mm)
1.3	0.72362	1.6	0.73288
1.3	0.80831	1.6	0.46964
1.3	1.57557	1.6	0.71014
1.3	1.00730	1.6	1.11897
1.3	0.85725	1.6	0.52933
1.3	1.08527	1.6	0.86274
1.3	1.33098	1.6	0.35045
1.3	1.63696	1.6	0.82148
1.3	1.10011	1.6	0.48866
1.3	1.16902	1.6	0.88298
1.4	0.85026	1.7	0.32390
1.4	1.18997	1.7	0.23234
1.4	0.94037	1.7	0.47694
1.4	1.26149	1.7	0.68112
1.4	0.88081	1.7	0.58937
1.4	0.99624	1.7	0.53654
1.4	0.75859	1.7	0.80040
1.4	0.75699	1.7	0.79617
1.4	0.68184	1.7	0.56005
1.4	0.91954	1.7	0.69631
1.5	1.05831	1.8	0.36181
1.5	0.64902	1.8	0.47093
1.5	1.01395	1.8	0.64245
1.5	0.71032	1.8	0.92319
1.5	0.72297	1.8	0.38581
1.5	0.63632	1.8	0.51473
1.5	0.66590	1.8	0.39712
1.5	0.59528	1.8	0.40665
1.5	1.06313	1.8	0.61757
1.5	0.72867	1.8	0.80856

Frequency (Hz)	Displacement (mm)
1.9	0.55967
1.9	0.41598
1.9	0.67828
1.9	0.80394
1.9	0.57495
1.9	0.29872
1.9	0.74848
1.9	0.36696
1.9	0.45144
1.9	0.96853
2.0	0.52730
2.0	0.61574
2.0	0.58303
2.0	0.37631
2.0	0.59885
2.0	0.41386
2.0	0.31662
2.0	0.48780
2.0	0.41443
2.0	0.57273

Appendix F.   0.003 Inch Diameter Wire Displacement Results

Frequency (Hz)	Displacement (mm)	Frequency (Hz)	Displacement (mm)
0.1	5.21354	0.4	3.20427
0.1	5.99176	0.4	3.86767
0.1	5.88097	0.4	3.65077
0.1	5.48993	0.4	3.70025
0.1	5.91830	0.4	3.78685
0.1	5.40136	0.4	3.49459
0.1	5.24544	0.4	3.78174
0.1	5.92659	0.4	3.51057
0.1	5.33544	0.4	3.88003
0.1	5.93410	0.4	3.32026
0.2	4.31751	0.5	3.67598
0.2	4.73591	0.5	3.30034
0.2	4.51734	0.5	3.77630
0.2	4.82336	0.5	3.02724
0.2	4.05312	0.5	3.65181
0.2	4.20595	0.5	3.71727
0.2	4.77342	0.5	3.37791
0.2	4.28384	0.5	3.52081
0.2	4.83700	0.5	3.51379
0.2	4.17577	0.5	3.65351
0.3	3.76961	0.6	3.27539
0.3	3.65033	0.6	3.50187
0.3	3.82007	0.6	3.17032
0.3	3.52541	0.6	2.93210
0.3	4.07084	0.6	3.13169
0.3	4.27732	0.6	2.94475
0.3	3.62153	0.6	3.23259
0.3	4.20396	0.6	3.03095
0.3	4.20441	0.6	3.43350
0.3	4.32086	0.6	3.33945

Frequency (Hz)	Displacement (mm)	Frequency (Hz)	Displacement (mm)
0.7	3.16713	1.0	2.82050
0.7	2.70365	1.0	2.55048
0.7	2.86286	1.0	3.04573
0.7	3.30002	1.0	3.12586
0.7	3.00652	1.0	2.90372
0.7	3.05784	1.0	2.90344
0.7	2.93218	1.0	3.13134
0.7	3.02517	1.0	2.74397
0.7	3.15258	1.0	2.71108
0.7	3.33044	1.0	3.04596
0.8	3.05702	1.1	2.77884
0.8	2.99718	1.1	2.79019
0.8	3.18161	1.1	2.60670
0.8	2.93658	1.1	2.84943
0.8	3.23648	1.1	2.30762
0.8	2.92924	1.1	2.58994
0.8	3.21434	1.1	2.68641
0.8	2.95945	1.1	2.92345
0.8	3.09575	1.1	2.12129
0.8	3.09377	1.1	2.87469
0.9	3.24914	1.2	1.62352
0.9	2.98734	1.2	2.00253
0.9	2.21388	1.2	1.59437
0.9	2.97706	1.2	2.03551
0.9	2.63245	1.2	2.49586
0.9	2.62324	1.2	3.05864
0.9	2.23585	1.2	1.58077
0.9	3.05993	1.2	1.93870
0.9	2.66004	1.2	2.99476
0.9	2.85238	1.2	2.82229

Frequency (Hz)	Displacement (mm)	Frequency (Hz)	Displacement (mm)
1.3	2.20069	1.6	1.00533
1.3	2.24432	1.6	1.76568
1.3	2.47544	1.6	1.40218
1.3	2.77223	1.6	0.74035
1.3	2.60728	1.6	1.92347
1.3	2.47294	1.6	1.29964
1.3	2.69654	1.6	2.28613
1.3	2.10615	1.6	0.91068
1.3	1.53102	1.6	1.80990
1.3	2.77828	1.6	2.39176
1.4	2.67826	1.7	1.02839
1.4	1.51988	1.7	2.21860
1.4	2.38435	1.7	1.81402
1.4	1.40698	1.7	1.27525
1.4	2.37235	1.7	0.98284
1.4	2.70989	1.7	1.72112
1.4	2.25145	1.7	1.09348
1.4	1.96499	1.7	1.15160
1.4	2.61251	1.7	0.75324
1.4	1.99606	1.7	1.28945
1.5	2.14161	1.8	1.48337
1.5	2.51311	1.8	0.98978
1.5	2.29477	1.8	2.04132
1.5	2.27389	1.8	1.06823
1.5	2.11900	1.8	1.11601
1.5	2.37945	1.8	1.42100
1.5	2.07091	1.8	0.99750
1.5	2.45118	1.8	0.89783
1.5	2.41072	1.8	1.15186
1.5	1.58060	1.8	1.26026

Frequency (Hz)	Displacement (mm)
1.9	1.46509
1.9	0.68585
1.9	0.76410
1.9	1.78974
1.9	1.37726
1.9	2.11316
1.9	1.46040
1.9	0.71624
1.9	1.21704
1.9	0.80807
2.0	0.68120
2.0	0.69721
2.0	1.13391
2.0	0.88063
2.0	1.13341
2.0	0.63223
2.0	0.71280
2.0	0.92714
2.0	0.55839
2.0	1.12747

Appendix G.   0.002 Inch Diameter Wire Displacement Results

Frequency (Hz)	Displacement (mm)	Frequency (Hz)	Displacement (mm)
0.1	6.07747	0.4	4.16354
0.1	6.14649	0.4	4.28436
0.1	6.08752	0.4	4.24081
0.1	5.99927	0.4	4.22524
0.1	5.81884	0.4	4.28185
0.1	5.87755	0.4	4.31482
0.1	6.27159	0.4	4.18019
0.1	6.30162	0.4	4.20060
0.1	6.07154	0.4	4.33609
0.1	6.08606	0.4	4.29510
0.2	4.97258	0.5	3.66021
0.2	5.08961	0.5	3.81244
0.2	4.88170	0.5	3.88743
0.2	4.88149	0.5	3.56602
0.2	4.85098	0.5	3.65043
0.2	5.02205	0.5	3.68527
0.2	4.84404	0.5	3.71081
0.2	5.22738	0.5	3.70967
0.2	5.02626	0.5	3.60591
0.2	4.88719	0.5	3.62325
0.3	4.62123	0.6	3.45725
0.3	4.54508	0.6	3.58972
0.3	4.50119	0.6	3.58168
0.3	4.33290	0.6	3.47522
0.3	4.44479	0.6	3.63664
0.3	4.42801	0.6	3.53762
0.3	4.40367	0.6	3.55236
0.3	4.63596	0.6	3.57765
0.3	4.51837	0.6	3.60464
0.3	4.42123	0.6	3.57158

Frequency (Hz)	Displacement (mm)	Frequency (Hz)	Displacement (mm)
0.7	3.46642	1.0	3.05514
0.7	3.50240	1.0	3.26290
0.7	3.44960	1.0	3.22255
0.7	3.50041	1.0	3.27366
0.7	3.49671	1.0	3.05973
0.7	3.44494	1.0	2.95423
0.7	3.43574	1.0	3.27650
0.7	3.45189	1.0	3.18428
0.7	3.53421	1.0	3.36925
0.7	3.47346	1.0	3.19356
0.8	3.58051	1.1	3.21976
0.8	3.40621	1.1	3.13442
0.8	3.47438	1.1	3.14834
0.8	3.43678	1.1	3.15971
0.8	3.45086	1.1	3.27131
0.8	3.48530	1.1	3.17125
0.8	3.40656	1.1	3.04007
0.8	3.47149	1.1	2.88842
0.8	3.45546	1.1	3.08688
0.8	3.41734	1.1	3.21280
0.9	3.02667	1.2	3.01812
0.9	3.43193	1.2	2.89979
0.9	3.20930	1.2	3.04143
0.9	3.34802	1.2	1.46506
0.9	3.15370	1.2	2.98809
0.9	3.30453	1.2	2.97994
0.9	3.30610	1.2	3.21754
0.9	3.34818	1.2	2.96818
0.9	3.32708	1.2	3.02706
0.9	3.36138	1.2	2.88807

Frequency (Hz)	Displacement (mm)	Frequency (Hz)	Displacement (mm)
1.3	3.05979	1.6	2.50308
1.3	2.40383	1.6	2.72380
1.3	2.70770	1.6	1.07983
1.3	2.79206	1.6	1.49843
1.3	2.87961	1.6	1.44112
1.3	2.75420	1.6	1.31074
1.3	2.97595	1.6	1.42136
1.3	2.93162	1.6	2.60308
1.3	2.64135	1.6	2.65189
1.3	2.68268	1.6	2.08166
1.4	2.15109	1.7	3.23082
1.4	2.18318	1.7	1.40690
1.4	2.74467	1.7	2.81714
1.4	2.42177	1.7	1.56564
1.4	1.54647	1.7	1.47839
1.4	1.35819	1.7	2.05386
1.4	1.84366	1.7	3.13614
1.4	2.78394	1.7	2.01347
1.4	2.45130	1.7	1.52809
1.4	2.66645	1.7	3.03105
1.5	1.87547	1.8	2.14475
1.5	1.86029	1.8	1.36858
1.5	1.28102	1.8	1.55736
1.5	2.23834	1.8	1.32629
1.5	1.09675	1.8	1.56237
1.5	1.78607	1.8	2.68930
1.5	2.11779	1.8	2.74025
1.5	2.30387	1.8	1.55953
1.5	1.18142	1.8	1.25801
1.5	2.34976	1.8	2.60257

Frequency (Hz)	Displacement (mm)
1.9	2.18576
1.9	2.16736
1.9	2.13226
1.9	1.33309
1.9	1.20254
1.9	2.12241
1.9	1.48002
1.9	1.60075
1.9	1.39200
1.9	2.18168
2.0	1.62656
2.0	1.28214
2.0	1.30983
2.0	1.23700
2.0	0.70572
2.0	1.90698
2.0	1.03628
2.0	1.63833
2.0	1.28288
2.0	1.34974

Appendix H.   0.0015 Inch Diameter Wire Displacement Results

Frequency (Hz)	Displacement (mm)	Frequency (Hz)	Displacement (mm)
0.1	4.76762	0.4	2.61652
0.1	4.65442	0.4	2.69056
0.1	5.08256	0.4	3.16564
0.1	4.04708	0.4	2.68415
0.1	4.04598	0.4	2.17338
0.1	4.73798	0.4	3.21520
0.1	5.21923	0.4	2.68226
0.1	4.10116	0.4	2.81877
0.1	5.11055	0.4	3.42292
0.1	4.66949	0.4	2.65881
0.2	4.18637	0.5	3.25505
0.2	3.11160	0.5	2.65493
0.2	3.16167	0.5	2.77478
0.2	4.30086	0.5	2.85409
0.2	3.06620	0.5	2.66849
0.2	3.16481	0.5	2.94455
0.2	3.86723	0.5	2.60063
0.2	4.24964	0.5	2.97750
0.2	4.04482	0.5	2.59772
0.2	3.27206	0.5	2.65909
0.3	2.97810	0.6	2.92850
0.3	2.67452	0.6	2.75275
0.3	3.35298	0.6	2.62941
0.3	2.86810	0.6	2.72845
0.3	2.63762	0.6	2.79737
0.3	3.58605	0.6	3.17513
0.3	3.12312	0.6	2.52823
0.3	3.23102	0.6	2.40800
0.3	2.51956	0.6	2.55624
0.3	2.49943	0.6	2.90301

Frequency (Hz)	Displacement (mm)	Frequency (Hz)	Displacement (mm)
0.7	2.57207	1.0	2.74006
0.7	2.68523	1.0	3.07136
0.7	2.94632	1.0	2.80098
0.7	2.82485	1.0	2.53484
0.7	2.82465	1.0	2.60868
0.7	2.99605	1.0	2.63924
0.7	3.22462	1.0	2.45263
0.7	2.85936	1.0	2.63489
0.7	2.66631	1.0	2.70459
0.7	2.68933	1.0	2.47113
0.8	2.42428	1.1	2.50250
0.8	2.85083	1.1	2.69201
0.8	2.73253	1.1	2.87171
0.8	2.69235	1.1	2.82179
0.8	3.05460	1.1	2.46897
0.8	3.09980	1.1	2.86820
0.8	2.98030	1.1	3.25964
0.8	2.77574	1.1	2.72752
0.8	2.78306	1.1	2.92461
0.8	2.83428	1.1	2.79888
0.9	2.78058	1.2	2.63522
0.9	2.78224	1.2	2.81058
0.9	2.77495	1.2	2.72616
0.9	2.73129	1.2	2.89479
0.9	2.71107	1.2	2.55359
0.9	2.99892	1.2	2.81616
0.9	3.09773	1.2	2.98755
0.9	2.74277	1.2	2.87045
0.9	2.72881	1.2	2.88991
0.9	2.83556	1.2	2.87308

Frequency (Hz)	Displacement (mm)	Frequency (Hz)	Displacement (mm)
1.3	3.09909	1.6	2.65887
1.3	2.98089	1.6	2.73861
1.3	3.02184	1.6	2.69204
1.3	2.93174	1.6	2.78673
1.3	2.37777	1.6	2.65108
1.3	2.29483	1.6	2.79328
1.3	2.57168	1.6	2.69680
1.3	2.98763	1.6	2.70347
1.3	2.64631	1.6	2.79837
1.3	2.89157	1.6	2.63465
1.4	2.96745	1.7	2.76155
1.4	2.21096	1.7	2.12429
1.4	2.67767	1.7	2.51030
1.4	3.02318	1.7	2.74916
1.4	2.74367	1.7	2.58636
1.4	2.50331	1.7	2.06392
1.4	2.82853	1.7	2.51910
1.4	2.55581	1.7	2.60463
1.4	2.92317	1.7	2.64826
1.4	2.37984	1.7	2.66586
1.5	2.38551	1.8	2.48488
1.5	2.72269	1.8	2.31240
1.5	2.61697	1.8	2.46053
1.5	2.69841	1.8	2.56290
1.5	2.78495	1.8	2.44157
1.5	2.60997	1.8	2.43752
1.5	2.61455	1.8	2.12834
1.5	2.90533	1.8	2.59597
1.5	2.61836	1.8	2.60888
1.5	2.62473	1.8	2.50103

Frequency (Hz)	Displacement (mm)
1.9	2.33784
1.9	2.36773
1.9	2.32495
1.9	2.42928
1.9	2.32076
1.9	2.39273
1.9	2.31152
1.9	2.09981
1.9	2.47290
1.9	2.36323
2.0	2.27792
2.0	2.02258
2.0	1.51157
2.0	2.26614
2.0	2.32480
2.0	1.62806
2.0	2.30751
2.0	2.35352
2.0	2.04610
2.0	2.32611

Appendix I. Component Masses

Component	Mass
Carbon Tubing (0.098 inch OD x 0.059 inch ID)	0.04561 g/cm
Carbon Tubing (0.08 inch OD x 0.04 inch ID)	0.03421 g/cm
26 gauge hypodermic tubing	0.00833 g/cm
22 gauge hypodermic tubing	0.01404 g/cm
0.0015 inch diameter wire	0.00012 g/cm
0.002 inch diameter wire	0.00015 g/cm
0.003 inch diameter wire	0.00028 g/cm
0.004 inch diameter wire	0.00047 g/cm
0.005 inch diameter wire	0.00080 g/cm
0.006 inch diameter wire	0.00110 g/cm
pushrod	0.0472 g/cm
Kwik-Link clevis (each)	0.303 g
bellcrank (each)	0.158 g
swivel clevis (each)	0.456 g
butt-splice	0.6949 g

Bibliography

Azuma, Akira. *The Biokinetics of Flying and Swimming, Second Edition*. Reston, VA: American Institute of Aeronautics and Astronautics Inc., 2006.

Birman, Victor. "Review of Mechanics of Shape Memory Alloy Structures," *Applied Mechanics Reviews*, 50: 629-645 (November 1997).

Brandreth, E. Judson Jr., "Airships: an Ideal Platform for Human or Remote Sensing in the Marine Environment," *Oceans 2000 MTS/IEEE Conference and Exhibition*, 3: 1883-5 (September 2000).

Dynalloy Incorporated. < http/dynalloy.com> Retrieved: August 2009.

Festo AG & Co. <http://www3.festo.com/__C1256D56002E7B89.nsf/html/ Air_ray_en.pdf/$FILE/Air_ray_en.pdf> Retrieved: February 2010.

Ho, Steven, Hanny Nassef, Nick Pornsinsirirak, Yu-Chong Tai, and Chih-Ming Ho. "Unsteady Aerodynamics and Flow Control for Flapping Wing Flyers," *Progress in Aerospace Sciences*, 39: 635-681 (November 2003).

Honma, Toshio. "Types and Mechanical Characteristics of Shape Memory Alloys," in *Shape Memory Alloys*. Ed. Hiroyasu Funakubo. New York: Gordon and Breach Science Publishers S.A. 1987.

Jadhav, Gautam. *The Development of a Miniature Flexible Flapping Wing Mechanism for use in a Robotic Air Vehicle.* MS thesis, Georgia Institute of Technology, Atlanta GA, March 2007.

Kohl, Manfred. *Shape Memory Microactuators.* Berlin: Springer, 2004.

Kroo, Ilan and Kunz, Peter "Mesoscale Flight and Miniature Rotorcraft Development," in *Fixed and Flapping Wing Aerodynamics for Micro Air Vehicle Applications.* Ed. Thomas J. Mueller. Reston, VA: American Institute of Aeronautics and Astronautics Inc., 2001.

Lan, Chao-Chieh, Jhe-Hong Wang, Chen-Hsien Fan. "Optimal Design of Rotary Manipulators Using Shape Memory Alloy Wire Actuated Flexures," *Sensors & Actuators A: Physical*, Vol 153, Issue 2: 258-266 (August 2009).

Liu, Tianshu. "Comparative Scaling of Flapping- and Fixed-Wing Flyers," American Institute of Aeronautics and Astronautics Journal, 44, Issue 1: 24-33 (January 2006).

McIntosh, Sean H., Agrawal, S., Khan, Z., "Design of a Mechanism for Biaxial Rotation of a Wing for a Hovering Vehicle," IEEE/ASME Transactions of Mechatronics, Vol. 11, No. 2, April 2006.

Michelson, R. C. "MicroFlyers and Aerial Robots: Missions and Design Criteria" Defense Technical Information Center Compilation Part Notice (ADP010759), 1999.

Mueller, Thomas J. and DeLaurier, James D. "An Overview of Micro Air Vehicle Aerodynamics," in *Fixed and Flapping Wing Aerodynamics for Micro Air Vehicle Applications.* Ed. Thomas J. Mueller, Reston, VA: American Institute of Aeronautics and Astronautics Inc., 2001.

Miyazaki, S. "Development and Characterization of Shape Memory Alloys," in *Shape Memory Alloys, CISM Courses and Lectures No. 351.* Ed. Carlo Tasso. New York: Springer-Verlag Wien New York, 1996.

Ohkata, Ichizo, and Yuichi Suzuki, "The Design of Shape Memory Alloy Actuators and Their Applications," in *Shape Memory Materials.* Ed. Kazuhiro Otsuka and C. Marvin Wayman, Cambridge: Cambridge University Press, 1998.

Rediniotis, Othon K. and Lagoudas, Dimitris C. "Shape Memory Alloy Actuators as Locomotor Muscles," in *Fixed and Flapping Wing Aerodynamics for Micro Air Vehicle Applications.* Ed. Thomas J. Mueller. Reston, VA: American Institute of Aeronautics and Astronautics Inc., 2001.

Seow, A. K., Yong Liu, W. K. Yeo, "Shape Memory Alloy Actuator to Deflect a Wing Flap," 49th AIAA/ASME/ASCE/ASC Structures, Structural Dynamics, and Materials Conference, Schaumburg, Illinois. April 2008.

Shimizu, Kenichi and Tadaki, Tsugio. "Shape Memory Effect: Mechanism," in *Shape Memory Alloys.* Ed. Hiroyasu Funakubo. New York: Gordon and Breach Science Publishers S.A. 1987.

Shyy, Wei; Lian, Yongsheng; Tang, Jian; Viieru, Dragos; and Liu, Hao. *Aerodynamics of Low Reynolds Number Flyers.* New York: Cambridge University Press, 2008.

Song, G., V. Chaudhry, C. Batur. "Precision Tracking Control of Shape Memory Alloy Actuators Using Neural Networks and a Sliding-Mode Based Robust Controller," *Smart Materials and Structures*, Vol 12, Issue 2: 223-231 (April 2003).

Spedding, G.R., P.B.S. Lissaman. "Technical Aspects of Microscale Flight Systems,"
    Journal of Avian Biology, Vol 29, Issue 4: 458-468 (December 1998).

Svanberg, Craig E. *Biometric Micro Air Vehicle Testing Development and Small Scale Flapping
    Wing Analysis.* MS Thesis, AFIT/GAE/ENY/08-M27. Graduate School of Engineering and
    Management, Air Force Institute of Technology (AU), Wright-Patterson AFB OH, March
    2008 (ADA478940).

Torres, Gabriel E. and Mueller, Thomas J. "Aerodynamic Characteristics of Low Aspect
    Ratio Wings At Low Reynolds Numbers," in *Fixed and Flapping Wing
    Aerodynamics for Micro Air Vehicle Applications.* Ed. Thomas J. Mueller.
    Reston, VA: American Institute of Aeronautic and Astronautics Inc., 2001.

Vita

LCDR Jeffery A. Barrett, USN is a native of Florence, Alabama. He graduated from The University of North Alabama with a Bachelor of Science degree, double major, in Physics and Chemistry. Completing Officer Candidate School in 1997, he received his commission as an officer in the United States Navy. Following flight school and designation as a Naval Aviator, he was assigned to VAQ-139 flying the EA-6B "Prowler". While assigned to VAQ-139, he made two carrier deployments and flew multiple combat missions including the initial weeks of Iraqi Freedom. Departing VAQ-139, he was assigned as an EA-6B instructor pilot and Landing Signal Officer at VAQ-129.

In 2009 LCDR Barrett was selected as an Aerospace Engineering Duty Officer. Following his graduation from AFIT, LCDR Barrett will report to PMA-234 (EA-6B Program Management Office) at Naval Air Station Patuxent River, Maryland.

REPORT DOCUMENTATION PAGE

Form Approved
OMB No. 0704–0188

The public reporting burden for this collection of information is estimated to average 1 hour per response, including the time for reviewing instructions, searching existing data sources, gathering and maintaining the data needed, and completing and reviewing the collection of information. Send comments regarding this burden estimate or any other aspect of this collection of information, including suggestions for reducing this burden to Department of Defense, Washington Headquarters Services, Directorate for Information Operations and Reports (0704–0188), 1215 Jefferson Davis Highway, Suite 1204, Arlington, VA 22202–4302. Respondents should be aware that notwithstanding any other provision of law, no person shall be subject to any penalty for failing to comply with a collection of information if it does not display a currently valid OMB control number. **PLEASE DO NOT RETURN YOUR FORM TO THE ABOVE ADDRESS.**

1. REPORT DATE (DD–MM–YYYY) 25-03-2010	2. REPORT TYPE Master's Thesis	3. DATES COVERED (From — To) May 2008 – March 2010

4. TITLE AND SUBTITLE Development of a Flapping Wing Design Incorporating Shape Memory Alloy Actuation	5a. CONTRACT NUMBER
	5b. GRANT NUMBER
	5c. PROGRAM ELEMENT NUMBER
6. AUTHOR(S) LCDR Jeffery A. Barrett, USN	5d. PROJECT NUMBER 09ENY152
	5e. TASK NUMBER
	5f. WORK UNIT NUMBER

7. PERFORMING ORGANIZATION NAME(S) AND ADDRESS(ES) Air Force Institute of Technology Graduate School of Engineering and Management (AFIT/ENY) 2950 Hobson Way WPAFB OH 45433-7765	8. PERFORMING ORGANIZATION REPORT NUMBER AFIT/GAE/ENY/10-M02

9. SPONSORING / MONITORING AGENCY NAME(S) AND ADDRESS(ES) Air Force Research Laboratory Air Vehicles Directorate AFRL/RBAA Dr. Greg Parker 2210 8th Street B146 R220 WPAFB OH 45433	10. SPONSOR/MONITOR'S ACRONYM(S) AFRL/RBAA
	11. SPONSOR/MONITOR'S REPORT NUMBER(S)

12. DISTRIBUTION / AVAILABILITY STATEMENT
APPROVED FOR PUBLIC RELEASE; DISTRIBUTION UNLIMITED

13. SUPPLEMENTARY NOTES

14. ABSTRACT

This research sought to validate a proof of concept regarding shape memory alloy actuation of a flapping-wing blimp. Specimen wires were subjected to cyclic voltage at increasing frequencies to quantify expected strains. A laser vibrometer captured 2048 sample velocities during single contraction and elongation cycles, and the resulting samples were used to calculate displacements. Displacements were determined ten times for each specimen and frequency to compute averages. Subsequently, a circumventing frame was designed to encase a blimp envelope and provide support for a flapping motion actuation system. Contraction of shape memory wire translated force to the flapping mechanism via bellcranks, pushrods, and clevises, while bias springs promoted elongation of the wire during power-off phases. Performance characteristics of the flapping system, augmented with each specimen wire individually, were determined during bench-top testing. A modified frame was constructed to reduce weight and fitted to a larger envelope due to buoyancy limitations of the original envelope. A circuit was constructed, cycling voltage at 0.2 hertz, to actuate the specimen wires. Performance of the system was observed with the incorporation of each specimen. Optimum performance was realized with the 0.005 inch diameter specimen wire, producing 25 to 35 degrees wing deflection.

15. SUBJECT TERMS
Shape Memory Alloy, Flapping Wing

16. SECURITY CLASSIFICATION OF:			17. LIMITATION OF ABSTRACT	18. NUMBER OF PAGES	19a. NAME OF RESPONSIBLE PERSON Dr. Jonathan T. Black, AFIT/ENY
a. REPORT	b. ABSTRACT	c. THIS PAGE	UU	111	19b. TELEPHONE NUMBER (Include Area Code) (937)255-3636, ext 4578
U	U	U			

Standard Form 298 (Rev. 8–98)
Prescribed by ANSI Std. Z39.18